# Fast computational optimization of TMS coil placement for individualized electric field targeting

Luis J. Gomez[1], Moritz Dannhauer[1], Angel V. Peterchev[1,2,3,4,#]
1 Department of Psychiatry and Behavioral Sciences, Duke University, NC, 27710, USA
2 Department of Electrical and Computer Engineering, Duke University, NC, 27708, USA
3 Department of Neurosurgery, Duke University, NC, 27710, USA
4 Department of Biomedical Engineering, Duke University, NC, 27708, USA

Emails: ljg24@duke.edu, moritz.dannhauer@duke.edu, and angel.peterchev@duke.edu

[#]Corresponding Author: Angel V. Peterchev
Address: 40 Duke Medicine Circle, Box 3620 DUMC, Durham, NC 27710, USA
Email: angel.peterchev@duke.edu
Phone: 919-684-0383

## Highlights

- Auxiliary dipole method (ADM) optimizes TMS coil placement in under 8 minutes
- Optimum orientations are near normal to the sulcal wall
- TMS induced E-field is less sensitive to orientation than position errors


## Abstract

*Background:* During transcranial magnetic stimulation (TMS) a coil placed on the scalp is used to non-invasively modulate activity of targeted brain networks via a magnetically induced electric field (E-field). Ideally, the E-field induced during TMS is concentrated on a targeted cortical region of interest (ROI).

*Objective:* To improve the accuracy of TMS we have developed a fast computational auxiliary dipole method (ADM) for determining the optimum coil position and orientation. The optimum coil placement maximizes the E-field along a predetermined direction or the overall E-field magnitude in the targeted ROI. Furthermore, ADM can assess E-field uncertainty resulting from precision limitations of TMS coil placement protocols, enabling minimization and statistical analysis of E-field dose variability.

*Method:* ADM leverages the reciprocity principle to rapidly compute the TMS induced E-field in the ROI by using the E-field generated by a virtual constant current source residing in the ROI. The framework starts by solving for the conduction currents resulting from this ROI current source. Then, it rapidly determines the average E-field induced in the ROI for each coil position by using the conduction currents and a fast-multipole method. To further speed-up the computations, the coil is approximated using auxiliary dipoles enabling it to represent all coil orientations for a given coil position with less than 600 dipoles.

*Results:* Using ADM, the E-fields generated in an MRI-derived head model when the coil is placed at 5,900 different scalp positions and 360 coil orientations per position can be determined in under 15 minutes on a standard laptop computer. This enables rapid extraction of the optimum coil position and orientation as well as the E-field uncertainty resulting from coil positioning uncertainty.

*Conclusion:* ADM enables the rapid determination of coil placement that maximizes E-field delivery to a specific brain target. This method can find the optimum coil placement in under 15 minutes enabling its routine use for TMS. Furthermore, it enables the fast quantification of uncertainty in the induced E-field due to limited precision of TMS coil placement protocols.



*Keywords* – transcranial magnetic stimulation, TMS, coil, targeting, E-field, model, optimal, reciprocity, auxiliary dipole method

# Introduction

Transcranial magnetic stimulation (TMS) is a noninvasive brain stimulation technique [1,2], where a TMS coil placed on the scalp is used to generate a magnetic field that induces an electric field (E-field) in the head. This, in turn, directly modulates the activity of brain regions and network nodes exposed to a high intensity E-field [3,4]. As such, computational E-field dosimetry has been identified by the National Institute of Mental Health as critical for identifying brain regions stimulated by TMS and for developing rigorous and reproducible TMS paradigms [5]. It is important to position and orient the coil to induce a maximal E-field on the targeted cortical region of interest (ROI) [6,7]. Furthermore, since coil placement protocols have limited precision, it is important to quantify variability in the TMS induced ROI E-field due to potential errors in coil placement. This work proposes the novel auxiliary dipole method (ADM) for fast E-field-informed optimal placement of the TMS coil and for quantifying uncertainty in the TMS induced E-field due to possible coil placement errors.

Optimal TMS coil placement is often determined by using scalp landmarks that correlate with targeted cortical ROIs. For example, to stimulate the dorsolateral prefrontal cortex (DLPFC), the coil is often positioned 5 cm anterior to a position that elicits motor evoked potentials in the contralateral hand muscle [8,9]. Alternatively, the coil is centered at a 10–20 coordinate location commonly used for EEG electrode positioning [10,11]. Scalp landmark-based strategies can result in significant misalignments between the coil placement and the targeted cortical ROI [12]. To improve coil placement, MRI imaging data is also sometimes used for ‘neuronavigated’ coil positioning. Standard neuronavigated protocols identify the location on the scalp directly over the targeted cortical site’s center of mass (CM) as the optimal coil center position [6,7,12]. This is because commonly used TMS coils have a figure-8 winding configuration that generates a primary E-field (E-field in the absence of the subject’s head) that is strongly concentrated

underneath its center [13]. However, the optimum coil placement site on the scalp can be shifted up to 12 mm (5.5 mm on average) away from the scalp location directly above the CM [14] by a secondary E-field generated inside the subject's head due to charge build-up on tissue interfaces [15-17].

The orientation of the TMS coil is typically chosen so that the direction of the induced E-field is perpendicular to the ROI's sulcal wall. This orientation is known to maximize the magnitude of the E-field in the ROI [14,18,19] and therefore corresponds to the lowest threshold for cortical activation, which is reinforced by the perpendicular orientation of the main axon of pyramidal neurons relative to the sulcal wall [4]. Indeed, E-field directed into the ROI sulcal wall requires, on average, lowest TMS coil currents to evoke a motor potential [20] and is close to the optimal orientation for targeting each region of the hand motor cortical area [14,21-23]. Therefore, in the absence of an explicit model of neural activation, choosing a coil position and orientation that maximizes the E-field strength is a suitable objective.

A further limitation of TMS procedures is that they have a limited, and often unquantified, precision and accuracy of determining and maintaining the coil placement. Even with gold-standard neuronavigation and robotic coil placement, coil position error can exceed 5 mm [24-26]. As such, there is an uncertainty in the TMS induced E-field resulting from uncertainty in the coil placement. This may result in variability in the outcomes of TMS interventions and needs to be quantified. Therefore, in addition to linking the external coil placement and current to the E-field induced in the brain, computational models should ideally account for coil placement uncertainty.

The total E-field induced in cortical ROIs can be determined by using MRI-derived subject-specific volume conductor models and finite element method (FEM) or boundary element method (BEM) [23,27-33]. Evaluating the TMS induced E-field for a single coil position using a standard

resolution head model currently requires 35 seconds using FEM [34] or 104 seconds using a fast-multipole method accelerated BEM [35]. Furthermore, E-field-informed optimal coil placement would require iterative execution of such simulations until an optimal coil position and orientation are found [36,37]. As such, computational requirements limit the routine use of E-field-informed optimization of coil placement. For example, for this reason we restricted the individual model-based dosing in a recent study to selecting only the coil current setting [37]. This paper introduces a computational approach that enables fast E-field-informed optimization of coil placement using high resolution individual head models. Our framework is exceptionally computationally efficient as it can evaluate the E-fields generated in a targeted cortical ROI using a standard MRI-derived head model when the coil is placed at 5,900 scalp different positions and 360 coil orientations per position in under 15 minutes using a laptop computer.

To determine the optimum coil placement on the scalp it is unnecessary to evaluate the E-field induced outside of the cortical ROI. This enables the use of the reciprocity principle to compute only the E-field induced in the ROI. Reciprocity has been used previously in the context of boundary element simulations of TMS induced E-fields [38,39]. These previous uses of reciprocity have two bottlenecks: First, they require the determination of either the magnetic field or E-field due to many electromagnetic point sources, which limits their use to low-resolution head discretizations. Second, they are limited to isotropic head models, and thus they cannot account for white matter tissue anisotropy. Here we avoid the low-resolution bottleneck by using a fast-multipole method (FMM) [40], which enables the rapid calculation of fields due to many electromagnetic point sources. Furthermore, to enable the use of anisotropic conductivity head models, we apply reciprocity by using directly conduction currents in the brain [41]. These modifications to previous uses of reciprocity in TMS modeling enable the use of head models from commonly adopted transcranial brain stimulation simulation pipelines [17,31] in our E-field-informed coil placement framework. Finally, we introduce a method for approximating the coil

currents by auxiliary dipoles enabling it to represent all coil orientations for a given coil position with less than 600 dipoles. This enables the rapid generation of maps that quantify the dependence of the E-field on both coil position and orientation. Furthermore, we post-process these maps to quantify the E-field uncertainty due to the limited accuracy and precision of coil placement methods.

The rest of this paper is structured as follows. First, we describe the proposed approachs to optimally locate and orient a TMS coil on the scalp to maximize E-field components in a brain ROI. Second, the approach is benchmarked in terms of accuracy relative to analytical solutions of a spherical head model and in terms of run-time and memory requirement relative to results obtained by directly using FEM to determine TMS induced E-fields. Third, we use a number of detailed realistic head models and target cortical ROIs from TMS experiments to compare the proposed method to placing the coil in a position that minimizes the scalp to cortical ROI distance. Finally, we use this approach to estimate quickly the E-field variation related to coil placement errors that inevitably occur with any TMS procedures.

Software implementations of the methods proposed in this paper are available for download [42]. for use in MATLAB and Python environments enabling easy integration with existing transcranial brain stimulation software packages (e.g., SimNIBS [43] and SCIRun [30]) as add-on toolkits.

## Methods

During TMS the coil placement is specified by the position of the coil center $\mathbf{R}$ and its orientation**,** which is indicated by a unit vector $\widehat{\mathbf{O}}$ that specifies the direction of the E-field directly under its center (Fig.1A). The average E-field along $\hat{\mathbf{t}}$ (i.e., $\langle \mathbf{E}(\mathbf{r}) \cdot \hat{\mathbf{t}} \rangle$, where $\langle \cdot \rangle$ computes the average over the ROI) and the average E-field magnitude (i.e., $\langle \| \mathbf{E}(\mathbf{r}) \| \rangle$) in a specified brain region of interest

(ROI) are both functions of coil position and orientation. We formulate the goal of optimal TMS coil placement to be the determination of a coil position $\mathbf{R_{opt}}$ and orientation $\hat{\mathbf{O}}_{\mathbf{opt}}$ that maximizes either $\langle \mathbf{E}(\mathbf{r}) \cdot \hat{\mathbf{t}} \rangle$ or $\langle \|\mathbf{E}(\mathbf{r})\| \rangle$. For example, $\langle \mathbf{E}(\mathbf{r}) \cdot \hat{\mathbf{t}} \rangle$ can be maximized if a preferential field alignment for the targeted neural population is known, whereas $\langle \|\mathbf{E}(\mathbf{r})\| \rangle$ is maximized whenever this information is missing.

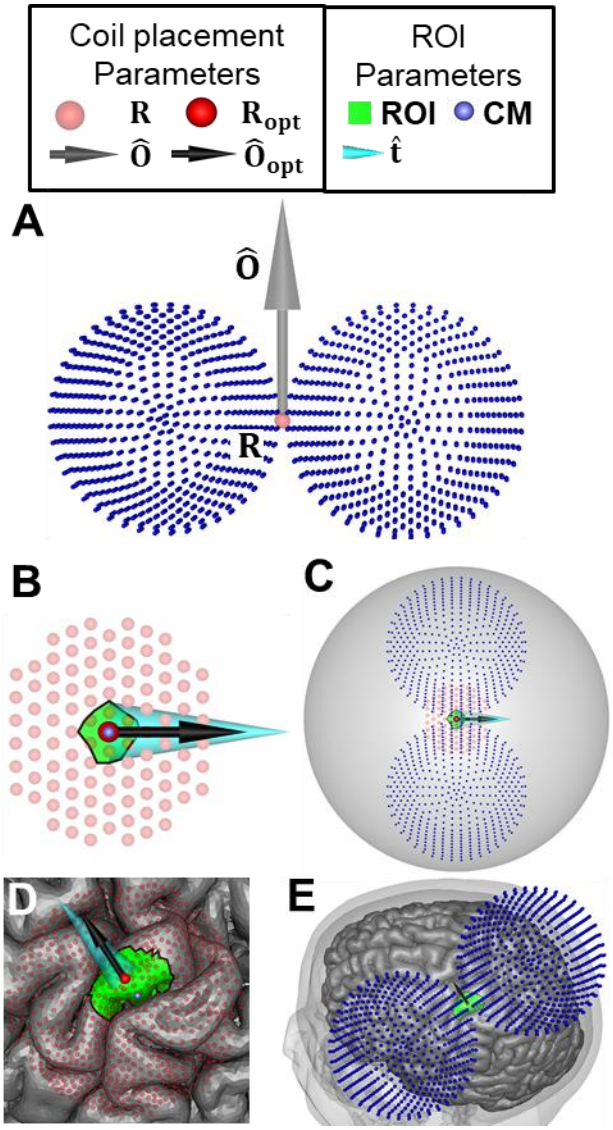


Figure 1. TMS coil placement. (A) A coil placement is identified by its central position $\mathbf{R}$ and the orientation, which is indicated by $\hat{\mathbf{O}}$. (B) Candidate coil positions for the spherical head model directly above the brain ROI. The optimum coil position is directly above CM and its orientation is aligned exactly with $\hat{\mathbf{t}}$. (C) Optimum figure-8 coil placement for a sphere head model. (D) Candidate coil positions for MRI-based (Ernie) head model directly above ROI. The optimum coil position and orientation differ slightly with the CM, and $\hat{\mathbf{t}}$ , respectively. (E) Optimum figure-8 coil placement for Ernie head model.

We describe a fast reciprocity-based method for evaluating $\langle \mathbf{E}(\mathbf{r}) \cdot \hat{\mathbf{t}} \rangle$. This method is used for rapid determination of $\mathbf{R}_{\mathbf{opt}}$ and $\widehat{\mathbf{O}}_{\mathbf{opt}}$ from a large number of candidate coil positions and orientations. Specifically, we set $\mathbf{R}_{\mathbf{opt}}$ and $\widehat{\mathbf{O}}_{\mathbf{opt}}$ as the candidate position and orientation that maximizes $\langle \mathbf{E}(\mathbf{r}) \cdot \hat{\mathbf{t}} \rangle$ (Figs. 1B–E). Furthermore, the method is extended to simultaneously determine the E-field direction $\hat{\mathbf{t}}_{\mathbf{opt}}$ and optimum coil position and orientation (i.e., $\mathbf{R}_{\mathbf{opt}}$ and $\widehat{\mathbf{O}}_{\mathbf{opt}}$) that maximizes $\langle \mathbf{E}(\mathbf{r}) \cdot \hat{\mathbf{t}} \rangle$. The simultaneous optimization of E-field direction and coil placement results in an optimum that also maximizes $\langle \|\mathbf{E}(\mathbf{r})\| \rangle$ in practical TMS targeting scenarios. This enables the ADM to also maximize the E-field magnitude in an ROI. For clarity we sometimes emphasize the dependence of $\langle \mathbf{E}(\mathbf{r}) \cdot \hat{\mathbf{t}} \rangle$ on coil position and orientation by referring to $\langle \mathbf{E}(\mathbf{r}) \cdot \hat{\mathbf{t}} \rangle$ as $\langle \mathbf{E}(\mathbf{r}) \cdot \hat{\mathbf{t}} \rangle(\mathbf{R}, \widehat{\mathbf{O}})$.

*Reciprocity method for determining* $\langle \mathbf{E}(\mathbf{r}) \cdot \hat{\mathbf{t}} \rangle$

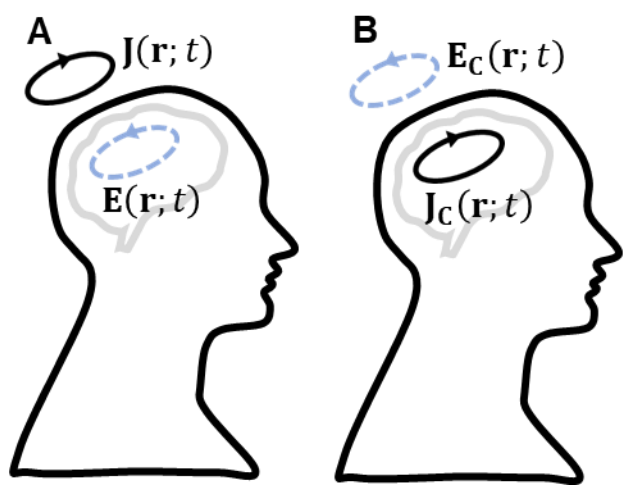


Figure 2. Reciprocal scenarios: (A) A TMS coil generates an E-field inside the brain. (B) A brain source generates an E-field where the coil resides.

Reciprocity is an equivalence relationship between two scenarios (Fig. 2). In one scenario, the TMS coil, modeled as impressed electric current $\mathbf{J}(\mathbf{r}; t) = p(t)\mathbf{J}(\mathbf{r})$, generates an E-field $\mathbf{E}(\mathbf{r}; t) = p'(t)\mathbf{E}(\mathbf{r})$ inside the head (Fig. 2A). Here $t$ is time, $\mathbf{r}$ is a Cartesian location, and $p(t)$ is the temporal variation and $p'(t)$ is the temporal derivative of the TMS current pulse. In the second

scenario, a source $\mathbf{J_C}(\mathbf{r};t) = p(t)\mathbf{J_C}(\mathbf{r})$ inside the head induces an E-field $\mathbf{E_C}(\mathbf{r};t) = p'(t)\mathbf{E_C}(\mathbf{r})$ in the TMS coil (Fig. 2B). Reciprocity dictates that the reaction integral between $\mathbf{E}(\mathbf{r};t)$ and $\mathbf{J_C}(\mathbf{r};t)$ is equal to the reaction integral between $\mathbf{J}(\mathbf{r};t)$ and $\mathbf{E_C}(\mathbf{r};t)$,

$$\int \mathbf{E}(\mathbf{r};\mathrm{t}) \cdot \mathbf{J_C}(\mathbf{r};\mathrm{t})\mathrm{d}\mathbf{r} = \int \mathbf{E_C}(\mathbf{r};\mathrm{t}) \cdot \mathbf{J}(\mathbf{r};\mathrm{t})\mathrm{d}\mathbf{r} \tag{1}$$

Here we choose $\mathbf{J_C}(\mathbf{r};t) = 0$ outside of the ROI and $\mathbf{J_C}(\mathbf{r};t) = p(t)V_{ROI}^{-1}\hat{\mathbf{t}}$ , where $V_{ROI}$ is the volume of the ROI, inside it. Reciprocity results the in average E-field along $\hat{\mathbf{t}}$ in the ROI being equal to

$$\langle \mathbf{E}(\mathbf{r}) \cdot \hat{\mathbf{t}} \rangle = V_{ROI}^{-1} \int_{\mathrm{ROI}} \mathbf{E}(\mathbf{r}) \cdot \hat{\mathbf{t}}\mathrm{d}\mathbf{r} = \int \mathbf{E_C}(\mathbf{r}) \cdot \mathbf{J}(\mathbf{r})\mathrm{d}\mathbf{r}, \tag{2}$$

Since for the TMS pulse waveform frequencies the E-field spatial and temporal components are separable (quasi-stationary) [44], the temporal variation of all currents and E-fields—$p(t)$ and $p'(t)$, respectively—is omitted in this and subsequent notation.

Computing $\langle \mathbf{E}(\mathbf{r}) \cdot \hat{\mathbf{t}} \rangle$ using Eq. (2) requires the evaluation of $\mathbf{E_C}(\mathbf{r})$ outside of the conductive head. This is done by computing the primary E-field due to the cortical current $\mathbf{J_C}(\mathbf{r})$ as well as the secondary E-field due to the conduction currents $\overline{\overline{\boldsymbol{\sigma}}}(\mathbf{r})\mathbf{E_C}(\mathbf{r})$, where $\overline{\overline{\boldsymbol{\sigma}}}(\mathbf{r})$ is the conductivity tensor inside the head. Thus,

$$\mathbf{E_C}(\mathbf{r}) = -\frac{\mu_0}{4\pi} \int_{\mathrm{Head}} \frac{\mathbf{J_C}(\mathbf{r}') + \overline{\overline{\boldsymbol{\sigma}}}(\mathbf{r}')\mathbf{E_C}(\mathbf{r}')}{\|\mathbf{r}-\mathbf{r}'\|} \mathrm{d}\mathbf{r}'. \tag{3}$$

Here $\mu_0$ is the permeability of free space, and the integration is done over the head domain. In the following section, we describe the FEM approach we used to compute $\mathbf{E_C}(\mathbf{r})$ inside the head, and numerical integration rules used to estimate Eqs. (2)–(3).

*Discretization of the reaction integral*

The E-field inside the head due to $\mathbf{J_C}(\mathbf{r})$ satisfies Laplace's equation, $\nabla \cdot \mathbf{J_C}(\mathbf{r}) = \nabla \cdot \overline{\overline{\boldsymbol{\sigma}}}(\mathbf{r})\nabla\phi(\mathbf{r})$,

where $\mathbf{E_C}(\mathbf{r}) = \nabla\phi(\mathbf{r})$. To solve for $\phi$ and $\nabla\phi$ we used an in-house 1nd order FEM method [33]. First, the head model is discretized into a tetrahedral mesh having $P$ nodes and $N$ tetrahedrons, and each tetrahedron is assigned a constant tissue conductivity tensor. Second, the scalar potential $\phi$ is approximated by piece-wise linear nodal elements $N_m(\mathbf{r})$ (where $m = 1, 2, \ldots, P$) [45]. Third, weak forms of Laplace's equation are sampled also using piecewise-linear nodal elements as testing functions in a standard Galerkin procedure. This results in

$$\begin{aligned}
&\mathbf{Ax} = \mathbf{b}, \\
&(\mathbf{A})_{m,n} = \int_{\mathbb{R}^3} \overline{\overline{\boldsymbol{\sigma}}}(\mathbf{r}) \nabla N_m(\mathbf{r}) \cdot \nabla N_n(\mathbf{r})\, \mathrm{d}\mathbf{r}, \\
&(\mathbf{b})_m = \frac{V_{ROI}^{-1}}{4\pi} \int_{\mathrm{ROI}} \hat{\mathbf{t}} \cdot \nabla N_m(\mathbf{r})\, \mathrm{d}\boldsymbol{r}, \\
&\mathbf{E_C}(\mathbf{r}) = -\sum_{m=1}^{P} (\mathbf{b})_m \nabla N_m(\mathbf{r}).
\end{aligned} \tag{4}$$

Entries $(\mathbf{A})_{m,n}$ are computed analytically using expressions provided in [45] and $\mathrm{ROI}$ denotes the support of $\mathbf{J_C}(\mathbf{r})$. The system of equations **Error! Reference source not found.** is solved using a transpose-free quasi-minimal residual [46] iterative solver to a relative residual of $10^{-10}$.

Samples of $\mathbf{E_C}(\mathbf{r})$ outside of the head are obtained via Eq. (3) and using the FEM solution. The volume cortical and conduction currents are approximated by current dipoles on the centroid of each tetrahedron. The current dipoles are computed as $\mathbf{J_C}^{(j)} = \left(\overline{\overline{\boldsymbol{\sigma}}}\left(\mathbf{r_C}^{(j)}\right)\mathbf{E_C}\left(\mathbf{r_C}^{(j)}\right) + \mathbf{J_C}\left(\mathbf{r_C}^{(j)}\right)\right) V_j$, where $\mathbf{r_C}^{(j)}$ is the centroid, and $V_j$ is the volume of the $j^{\text{th}}$ tetrahedron. When the above conduction current approximation is applied to Eq. (3), it yields the following

$$\mathbf{E_C}(\mathbf{r}) = -\frac{\mu_0}{4\pi} \sum_{j=1}^{N} \frac{\mathbf{J_C}^{(j)}}{\left\|\mathbf{r} - \mathbf{r_C}^{(j)}\right\|}. \tag{5}$$

Typically coil models consist of dipoles $\mathbf{J_{coil}}^{(i)}$ at locations $\mathbf{r_{coil}}^{(i)}$ , where $i = 1,2, \ldots, M$. As a result, using a coil dipole model and Eq. (5) to evaluate Eq. (2) results in

$$\langle \mathbf{E}(\mathbf{r}) \cdot \hat{\mathbf{t}} \rangle = -\frac{\mu_0}{4\pi} \sum_{i=1}^{M} \mathbf{J_{coil}}^{(i)} \cdot \sum_{j=1}^{N} \frac{\mathbf{J_C}^{(j)}}{\left\|\mathbf{r_{coil}}^{(i)} - \mathbf{r_C}^{(j)}\right\|}. \tag{6}$$

Evaluating Eq. (5) at a single position requires evaluating the sum of $N$ entries (i.e., the number of computations scales with the number of tetrahedrons). Furthermore, computing $\langle \mathbf{E}(\mathbf{r}) \cdot \hat{\mathbf{t}} \rangle$ using Eq. (6) requires the evaluation of Eq. (5) at $M$ positions (i.e., the number of computations scales with the number of tetrahedrons times the number of coil model dipoles $M \times N$). If one wants to evaluate $\langle \mathbf{E}(\mathbf{r}) \cdot \hat{\mathbf{t}} \rangle$ for $L$ different coil placements, the number of computations will scale as $L \times M \times N$. As a result, there are trade-offs between how large $L$, $M$, and $N$ can be while maintaining a tractable number of computations. For example, if the number of tetrahedrons is large we are limited in the number of coil placements for which we can evaluate the E-field. Conversely, if we would like to evaluate the E-field for many coil placements, the resolution of the head model has to be lowered. This is a common limitation of reciprocity based E-field BEM solvers for TMS [38,39]. To lower the computational cost, we use the fast-multipole method (FMM), which was designed to lower the computational complexity of the calculation of Eq. (6). Specifically, it reduces the total computation from scaling as $N \times M \times L$ to scaling as the maximum between $N$ and $M \times L$. Using FMM enables us to compute Eq. (6) with both dense head meshes (i.e., large $N$) and for many coil placements (i.e., large $M \times L$). Furthermore, in the supplemental material we describe an auxiliary dipole model generation used here that leverages the same set of dipole locations for multiple coil orientations further speeding up our method. Note the method as presented here does not work with magnetic dipole TMS coil models. Its extension to magnetic sources requires minor modifications given in the supplemental material. Software implementations for both electric and magnetic dipole sources are available in [42].

*Simultaneously optimizing coil placement and E-field direction*

For each candidate coil position and orientation, the reciprocity based method is run three times to compute $\langle \mathbf{E}(\mathbf{r}) \cdot \hat{\mathbf{x}} \rangle(\mathbf{R}, \widehat{\mathbf{O}})$, $\langle \mathbf{E}(\mathbf{r}) \cdot \hat{\mathbf{y}} \rangle(\mathbf{R}, \widehat{\mathbf{O}})$, and $\langle \mathbf{E}(\mathbf{r}) \cdot \hat{\mathbf{z}} \rangle(\mathbf{R}, \widehat{\mathbf{O}})$. From these three principal directions we can compute any $\langle \mathbf{E}(\mathbf{r}) \cdot \hat{\mathbf{t}} \rangle(\mathbf{R}, \widehat{\mathbf{O}})$ using the linear decomposition $\langle \mathbf{E}(\mathbf{r}) \cdot \hat{\mathbf{t}} \rangle(\mathbf{R}, \widehat{\mathbf{O}}) =$

$(\hat{\mathbf{t}} \cdot \hat{\mathbf{x}})\langle \mathbf{E}(\mathbf{r}) \cdot \hat{\mathbf{x}} \rangle(\mathbf{R}, \widehat{\mathbf{O}}) + (\hat{\mathbf{t}} \cdot \hat{\mathbf{y}})\langle \mathbf{E}(\mathbf{r}) \cdot \hat{\mathbf{y}} \rangle(\mathbf{R}, \widehat{\mathbf{O}}) + (\hat{\mathbf{t}} \cdot \hat{\mathbf{z}})\langle \mathbf{E}(\mathbf{r}) \cdot \hat{\mathbf{z}} \rangle(\mathbf{R}, \widehat{\mathbf{O}})$. The linear decomposition of indicates that $\langle \mathbf{E}(\mathbf{r}) \cdot \hat{\mathbf{t}} \rangle(\mathbf{R}, \widehat{\mathbf{O}})$ is maximum whenever $\hat{\mathbf{t}}$ is chosen as $\langle \widehat{\mathbf{E}(\mathbf{r})} \rangle = \langle \mathbf{E}(\mathbf{r}) \rangle(\mathbf{R}, \widehat{\mathbf{O}}) / \left\| \langle \mathbf{E}(\mathbf{r}) \rangle(\mathbf{R}, \widehat{\mathbf{O}}) \right\|$. As such, $\hat{\mathbf{t}}_{\mathbf{opt}} = \langle \widehat{\mathbf{E}(\mathbf{r})} \rangle(\mathbf{R}_{\mathbf{opt}}, \widehat{\mathbf{O}}_{\mathbf{opt}})$ and $\mathbf{R}_{\mathbf{opt}}$ and $\widehat{\mathbf{O}}_{\mathbf{opt}}$ should be chosen to maximize $\langle \mathbf{E}(\mathbf{r}) \rangle \cdot \langle \widehat{\mathbf{E}(\mathbf{r})} \rangle = \| \langle \mathbf{E}(\mathbf{r}) \rangle \| = \sqrt{\langle \mathbf{E}(\mathbf{r}) \cdot \hat{\mathbf{x}} \rangle^2 + \langle \mathbf{E}(\mathbf{r}) \cdot \hat{\mathbf{y}} \rangle^2 + \langle \mathbf{E}(\mathbf{r}) \cdot \hat{\mathbf{z}} \rangle^2}$.

Oftentimes, it is desired to maximize the average E-field magnitude in the ROI

$$\langle \| \mathbf{E}(\mathbf{r}) \| \rangle = V_{ROI}^{-1} \int_{\mathrm{ROI}} \mathbf{E}(\mathbf{r}) \cdot \left( \frac{\mathbf{E}(\mathbf{r})}{\| \mathbf{E}(\mathbf{r}) \|} \right) \mathrm{d}\mathbf{r}. \tag{7}$$

For a given coil position $\mathbf{R}$ and $\widehat{\mathbf{O}}$ the best possible approximation of $\langle \| \mathbf{E}(\mathbf{r}) \| \rangle$ that can be obtained while replacing unit vector $\frac{\mathbf{E}(\mathbf{r})}{\| \mathbf{E}(\mathbf{r}) \|}$ by a constant unit vector is $\langle \| \mathbf{E}(\mathbf{r}) \| \rangle \approx \| \langle \mathbf{E}(\mathbf{r}) \rangle \|$. In other words, instead of computing the magnitude and then taking the average over the ROI, the average is first computed and then the magnitude is taken. This approximation is valid whenever the E-field in the ROI is nearly unidirectional. As such, the approximation will be less accurate for larger ROIs relative to smaller ones. We compared results obtained by directly computing $\langle \| \mathbf{E}(\mathbf{r}) \| \rangle$ with ones for $\| \langle \mathbf{E}(\mathbf{r}) \rangle \|$ for ROIs of varying sizes to assess the accuracy of this approximation. Furthermore, we ran SimNIBS [47] coil placement optimization to maximize $\langle \| \mathbf{E}(\mathbf{r}) \| \rangle$ and compared with our results obtained by maximizing $\| \langle \mathbf{E}(\mathbf{r}) \rangle \|$.

*Head modeling*

For numerical validation of the method we employed SimNIBS example spherical shell and Ernie MRI-derived head model meshes. The spherical head mesh consists of a homogenous compartment with radius of 9.5 cm and conductivity of 0.33 S/m. The SimNIBS v3.1 Ernie head model mesh [18] consists of five homogenous compartments including white matter, gray matter, cerebrospinal fluid, skull, and skin. The scalp, skull, and cerebrospinal fluid conductivities were set to isotropic values of 0.465, 0.010, and 1.654 S/m, respectively. The gray and white matter

compartments were assigned anisotropic conductivities to account for the fibered tissue structure. This was accomplished within SimNIBS by co-registering the diffusion-weighted imaging data employing a volume normalization of the brain conductivity tensor, where the geometric mean of the tensor eigenvalues was set to the default isotropic conductivities of 0.275 and 0.126 S/m for gray and white matter, respectively.

Additional MRI-based head models—M1, M2, M3, and M4—were borrowed from one of our experimental studies involving E-field-based dosing [37], corresponding subject ids are S262, S263, S266, and S269. Briefly, the models were constructed using structural T1-weighted (echoplanar sequence: Voxel Size= 1 $mm^3$, TR= 7.148 ms, TE = 2.704 ms, Flip Angle = 12°, FOV = 256 $mm^2$, Bandwidth = 127.8 Hz/pixel), T2-weighted (echo-planar sequence with fat saturation: Voxel Size = 0.9375 × 0.9375 × 2.0 $mm^3$, TR = 4 s, TE = 77.23 ms, Flip Angle = 111°, FOV = 240 mm2, Bandwidth = 129.1 Hz/pixel), and diffusion-weighted scans (Single-shot echo-planar: Voxel Size = 2 $mm^3$, TR = 17 s, TE = 91.4 ms, Flip Angle = 90°, FOV = 256 $mm^2$, Bandwidth = 127.8 Hz/pixel, Matrix size = 1282, B-value = 2000 s/$mm^2$, Diffusion directions = 26). Each model was first generated employing the co-registered T1- and T2-weighted MRI data sets to model major head tissues (scalp, skull, cerebrospinal fluid, gray and white brain matter) represented as tetrahedral mesh elements. The number of tetrahedral mesh elements and nodes were ranged 0.679–0.699 million and 3.82–3.92 million, respectively. Mesh conductivities were assigned following the same procedure as for the SimNIBS Ernie model.

*Coil modeling*

The 2712 magnetic dipole model of the Magstim 70 mm figure-8 coil (P/N 9790) [48] included in SimNIBS (dI/dt = 1 A/μs) was used for all simulations. In its native space this coil is flat on the x–y plane, centered about the z axis. For all SimNIBS simulations, we used precomputed magnetic vector potentials of the chosen coil which is available within the package (file:

‘Magstim_70mm_Fig8.nii.gz’) to keep computation times as small as possible for exhaustive applications.

To speed-up computation further, we generate auxiliary coil models each modeling a distinct coil orientation. The dipole locations are the same across different auxiliary coil models, and coil models only differ in terms of their dipole weights. As a result, we can rapidly determine E-fields for many coil orientations each time using the same E-field samples outside of the head. In particular, we generated 360 models by rotating the coil dipole model around the z axis (0° to 359° in steps of 1°), as described in the supplemental material. All auxiliary dipole models share the same dipole locations on a $N_x \times N_y \times N_z$ grid of points. The total number of auxiliary dipoles is 578 and grid parameters were chosen as $N_x = N_y = 17$ and $N_z = 2$. To test the ADM, we used the SimNIBS Ernie example model and evaluated auxiliary coil dipole models consisting of all possible combinations of $N_x = N_y$ varying from 1 to 29, and $N_z$ varying from 1 to 3.

*ROI and grid generation*

For the spherical head, we considered a 2 cm diameter ROI centered 1.5 cm directly below the apex of the sphere as shown in Fig. 1C. A number of coil placements were chosen on a 2 cm diameter grid of 3.7–4.2 mm spaced positions and centered 4 mm above the apex of the sphere (Fig. 1C). For each coil placement, the coil was oriented tangentially to the sphere surface and different orientations where chosen by counterclockwise angular displacements 0°, 45° ,90°, and 135° relative to $\hat{\mathbf{x}} \times \hat{\mathbf{r}}$. In other words, candidate orientations $\widehat{\mathbf{O}}$ are $\hat{\mathbf{v}}_{\mathbf{1}}\cos(\theta_i) + \hat{\mathbf{v}}_{\mathbf{2}}\sin(\theta_i)$, where $\theta_i$ is either 0°, 45° ,90°, and 135°, $\hat{\mathbf{v}}_{\mathbf{1}} = \hat{\mathbf{r}} \times \hat{\mathbf{x}}/\|\hat{\mathbf{r}} \times \hat{\mathbf{x}}\|$, $\hat{\mathbf{v}}_{\mathbf{2}} = \hat{\mathbf{r}} \times \hat{\mathbf{v}}_{\mathbf{1}}$ and $\hat{\mathbf{r}}$ is the unit vector in the radial direction.

For the Ernie head model, the ROI was chosen as the gray matter contained in a 1 cm diameter

cubic region centered about location (−55.1, −18.0, 96.4) as shown in Fig. 1D,E. Coil placements were chosen by extracting mesh nodes on the scalp that were within a 2 cm diameter of the point on the scalp closest to the centroid of the brain ROI and then projecting the nodes 4 mm outward in direction normal to the scalp surface. For each of the 632 coil placements (Fig. 1D), the coil was placed tangent to the scalp and different orientations where chosen by counterclockwise angular displacements 0°, 45°, 90°, and 135° relative to $\hat{\mathbf{v}}_1 = \hat{\mathbf{x}} - (\hat{\mathbf{x}} \cdot \hat{\mathbf{n}})\hat{\mathbf{n}} / \|\hat{\mathbf{x}} - (\hat{\mathbf{x}} \cdot \hat{\mathbf{n}})\hat{\mathbf{n}}\|$, where $\hat{\mathbf{n}}$ is the unit normal on the scalp directly below the center of the coil.

For each of the four additional models (M1–M4), four ROIs where generated using the SimNIBS TMS coil placement optimization functionality with diameter of 0.1, 1, 2, and 4 cm (ROI1, ROI2, ROI3, ROI4) derived from fMRI-measured brain activity [37]. The smallest diameter ROIs consist of a single tetrahedron and we defined the diameter for these ROIs as the equivalent sphere diameter $2\left(\frac{3}{4\pi}V_{ROI}^{-1}\right)^{1/3}$ the mean diameter, across the four subjects, is 1.0 mm. SimNIBS was used to generate coil center positions on 3 cm diameter scalp region centered about the scalp position closest to the ROIs CM [37]. Each coil position was chosen to be approximately 1 mm apart and scalp positions where extruded outward by an amount dependent on the individual hair thicknesse: 3.26, 2.03, 5.55, and 2.78 mm for models M1–M4, respectively [37]. For each position, we used the direct approach with SimNIBS and the reciprocity-based ADM to generate, respectively, 72 and 360 coil orientations tangent to the scalp by rotating the coil in 5° and 1° intervals about the scalp normal direction. For each of the MRI-based head models $\hat{\mathbf{t}}$ is chosen as $\hat{\mathbf{t}}_{\mathbf{opt}}$.

*Visualizations*

In this work, all visualizations of anatomical details of the used volume conductor models, TMS coil setups/optimizations and E-Field distributions are generated with SCIRun (v4.7, R45838; [30], Fig. 1/9 and parts of Fig. 10/11) and MATLAB R2019 (Mathworks, Natick, MA, USA; Fig. 3-

7,10/11).

*Error metrics*

For each optimization setup we consider a normalized absolute error metric, which is normalized to the maximum observed $\langle \mathbf{E}(\mathbf{r}) \cdot \hat{\mathbf{t}} \rangle$,

$$err_{i,j} = \frac{\left| \langle \mathbf{E}(\mathbf{r}) \cdot \hat{\mathbf{t}} \rangle \left( (\mathbf{R})_i, (\hat{\mathbf{O}})_j \right) - \langle \mathbf{E}_{\mathbf{REF}}(\mathbf{r}) \cdot \hat{\mathbf{t}} \rangle \left( (\mathbf{R})_i, (\hat{\mathbf{O}})_j \right) \right|}{\left| \langle \mathbf{E}_{\mathbf{REF}}(\mathbf{r}) \cdot \hat{\mathbf{t}} \rangle (\mathbf{R}_{\mathbf{opt}} \hat{\mathbf{O}}_{\mathbf{opt}}) \right|}, \tag{8}$$

where $\langle \mathbf{E}(\mathbf{r}) \cdot \hat{\mathbf{t}} \rangle \left( (\mathbf{R})_i, (\hat{\mathbf{O}})_j \right)$ and $\langle \mathbf{E}_{\mathbf{REF}}(\mathbf{r}) \cdot \hat{\mathbf{t}} \rangle \left( (\mathbf{R})_i, (\hat{\mathbf{O}})_j \right)$ are the average E-fields computed by one of our proposed method and a reference method, respectively, for the $i^{th}$ candidate coil position and $j^{th}$ orientation. Additionally, we compare the E-field magnitude estimate $\| \langle \mathbf{E}(\mathbf{r}) \rangle \|$ to $\langle \| \mathbf{E}(\mathbf{r}) \| \rangle$ normalized to the maximum observed$\langle \| \mathbf{E}(\mathbf{r}) \| \rangle$

$$errMag_{i,j} = \frac{\left| \| \langle \mathbf{E}(\mathbf{r}) \rangle \| \left( (\mathbf{R})_i, (\hat{\mathbf{O}})_j \right) - \langle \| \mathbf{E}(\mathbf{r}) \| \rangle \left( (\mathbf{R})_i, (\hat{\mathbf{O}})_j \right) \right|}{\langle \| \mathbf{E}(\mathbf{r}) \| \rangle (\mathbf{R}_{\mathbf{opt}} \hat{\mathbf{O}}_{\mathbf{opt}})}. \tag{9}$$

*Coil placement uncertainty quantification*

Using the reciprocity technique, we can also compute uncertainty in the E-field resulting from coil placement uncertainty. First, we use the reciprocity method to construct maps indicating the E-field induced for all possible coil positions and orientations on the considered region of the scalp. Second, this map is used to extract uncertainty of the E-field induced during TMS resulting from uncertainty in coil placement.

Uncertainty in coil placement is modeled as a probability distribution describing the likelihood of the coil being placed with a given orientation and location on the scalp. Here we assume that the coil position and orientation are uniformly distributed random variables with distributions centered at the nominal scalp position $\mathbf{R}_{\boldsymbol{\mu}}$ and coil orientation $\hat{\mathbf{O}}_{\boldsymbol{\mu}}$. The support of the distribution comprises the scalp region within a geodesic distance $R_{\Delta}$ from $\mathbf{R}_{\boldsymbol{\mu}}$ and all coil orientation deviations up to $\theta_{\Delta}$ from $\hat{\mathbf{O}}_{\boldsymbol{\mu}}$. Specifically, the support is

$$\Omega_{coil} = \left\{ \left(\mathbf{R}, \widehat{\mathbf{O}}\right) \middle| \left\| \mathbf{R} - \mathbf{R}_{\boldsymbol{\mu}} \right\|_{\boldsymbol{g}} \leq R_{\Delta} \,; \widehat{\mathbf{O}} \; = \widehat{\mathbf{O}}_{\boldsymbol{\mu}} \; \cos(\theta) + \widehat{\mathbf{n}} \times \widehat{\mathbf{O}}_{\boldsymbol{\mu}} \; \sin(\theta) \;\; |\theta| \leq \theta_{\Delta} \right\}, \qquad (10)$$

where $\left\| \mathbf{R} - \mathbf{R}_{\boldsymbol{\mu}} \right\|_{\boldsymbol{g}}$ is the geodesic distance along the scalp between $\mathbf{R}$ and $\mathbf{R}_{\boldsymbol{\mu}}$, and parameters $R_{\Delta}$ and $\theta_{\Delta}$ are radii of the positional and angular support of the distribution. The values of $R_{\Delta}$ and $\theta_{\Delta}$ are specific to the TMS methods used and should be based on available data [24-26]. Furthermore, other distributions (e.g., Gaussians) can also be used to discretize the coil position and orientation uncertainty whenever appropriate. The geodesic distance on the scalp is computed using the heat method described in [49].

## Results

*Validation studies*

For the spherical head model, we compare the average E-field in the ROI predicted by our in-house direct FEM, reciprocity, and ADM with the analytically computed value. The average E-field analytically computed for each coil placement is shown in Fig. 3. As expected, the maximum occurs when the coil is placed directly above the ROI and oriented to induce a maximum primary E-field along $\hat{\mathbf{t}}$. The errors normalized to the maximum E-field across all simulations is shown in Fig. 3. The maximum error obtained for the direct FEM, reciprocity, and ADM are 0.06 %, 0.08 %, and 0.46 %, respectively. There is a slightly reduced accuracy in the ADM relative to the direct FEM and reciprocity approaches. However, errors are still significantly low with the ADM indicating that 578 dipoles are sufficient to accurately represent the coil fields for all the test cases. These simulations where also run in SimNIBS and we observed maximum error for SimNIBS simulations of 0.16%. Additional SimNIBS error figures are given in the supplemental material.

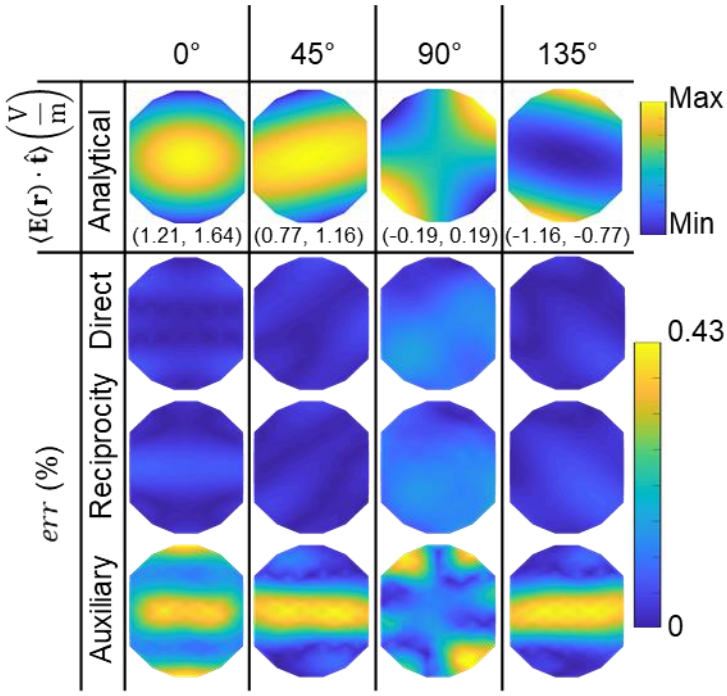


Figure 3. Validation of the computational methods in sphere head model. The 1st row shows, as a reference, the analytically computed average ROI E-field in direction $\hat{\mathbf{t}}$ (oriented horizontally) across TMS coil positions on the scalp. The scalp area spanned by the coil positions has a diameter of 2 cm. Four coil orientations are considered, from left to right: 0°, 45°, 90°, and 135°. The range of observed E-field component values are given in parenthesis below each figure in V/m. The 2nd, 3rd, and 4th row contain the corresponding absolute error relative to the analytical solution, $err$, for the direct, reciprocity, and ADM approaches, respectively.

For the Ernie head model, we compare the average E-field in the ROI predicted by the in-house direct FEM, reciprocity, and ADM. The value of $\hat{\mathbf{t}}$ is chosen (as described above) as $(-0.57, -0.72, -0.39)$ by evaluating the E-field for coil orientations varying from 0° to 359° in 5° intervals at each of the coil positions. The average E-field computed by the direct FEM for each coil position is shown in Fig. 4, and a maximum E-field is obtained when the coil is placed 4.5 mm away from the point on the grid closest to the ROI center of mass. The normalized absolute error of the different approaches, when using direct FEM as reference, is shown in Fig. 4. All approaches agree with the direct FEM and have relative absolute errors below 0.13%. The maximum normalized absolute errors across all simulations of the ADM relative to the reciprocity approach is shown in Fig. 5. The ADM converges to the reciprocity results exponentially with increasing number of dipoles, and an error below 0.5% is observed using the configuration of 578

dipoles. Additional comparisons with SimNIBS results given in the supplemental material have a maximum relative error below 0.11 %.

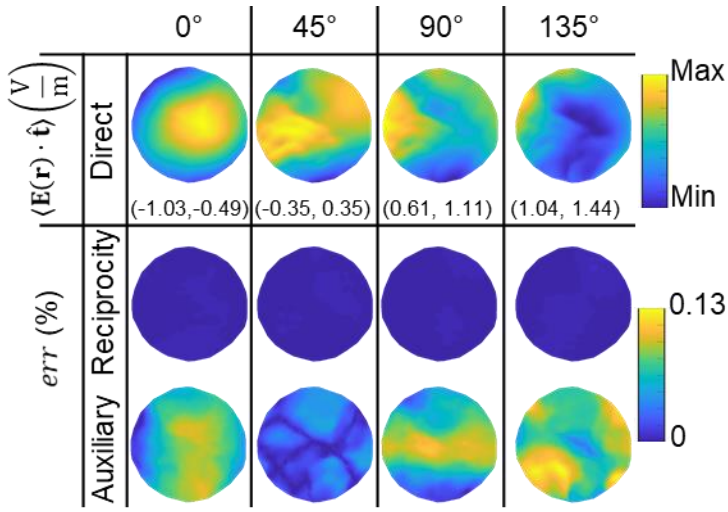


Figure 4. Validation in the Ernie head model, analogous to Fig. 4. The 1st row shows, as a reference, the directly computed average ROI E-field in direction $\hat{\mathbf{t}}$ (oriented horizontally) across TMS coil positions on the scalp. The 1st row shows, as a reference, the directly computed average ROI E-field at each scalp location. The scalp area spanned by the coil positions has a diameter of 2 cm. Four coil orientations are considered, from left to right: 0°, 45°, 90°, and 135°. The range of observed E-field component values are given in parenthesis below each figure in V/m. The 2nd and 3rd row contain the corresponding error relative to the direct approach, $err$, for the reciprocity and ADM approaches, respectively. The direct approach is used as a reference since there is no analytical solution for anatomically-detailed MRI-based head models.

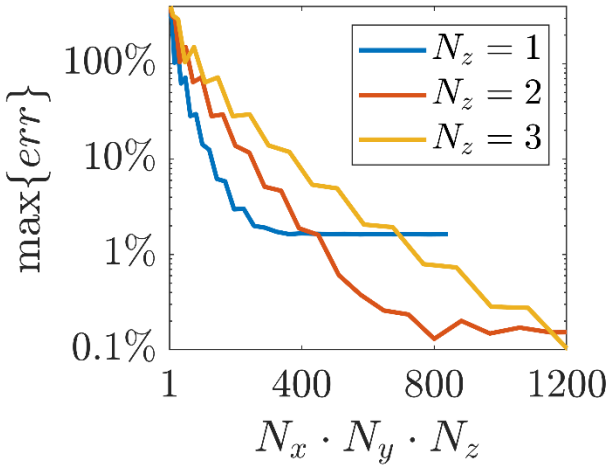


Figure 5. Maximum normalized absolute error when using auxiliary dipole models relative to the reciprocity results as a function of number of auxiliary dipoles.

For the four models (M1–M4) we compare metric $\langle \|\mathbf{E}(\mathbf{r})\| \rangle$ to $\|\langle \mathbf{E}(\mathbf{r}) \rangle\|$ for ROIs of varying sizes. Fig. 6 shows the maximum magnitude error obtained by comparing the ADM to compute $\|\langle \mathbf{E}(\mathbf{r}) \rangle\|$ relative to using direct FEM to compute $\langle \|\mathbf{E}(\mathbf{r})\| \rangle$ for ROIs of varying sizes. The maximum error

increases with increasing ROI size. From what is known of the spatial resolution of TMS experimentally, the diameter of a typical ROI is below 1 cm diameter, and for these sizes the errors are below 0.5 %. For larger ROIs with diameters between 1 cm and 2 cm the error is still below 2.0 %. These results indicate that $\langle \|\mathbf{E}(\mathbf{r})\| \rangle$ can be approximated by $\|\langle \mathbf{E}(\mathbf{r}) \rangle\|$ in many practical TMS settings.

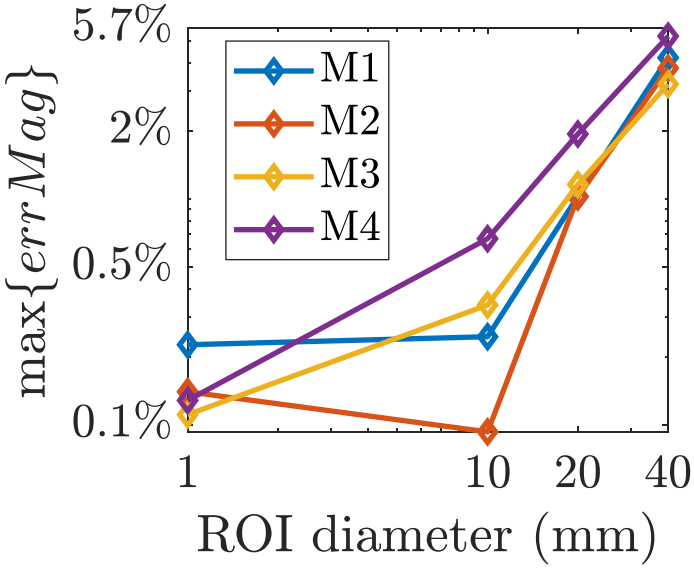


Figure 6. Maximum E-field magnitude estimate error (Eq. (9)) using ADM to the reciprocity results as a function of ROI diameter.

*Computational runtime and memory*

Coil placement optimizations were run each time using a different number of candidate designs. The optimizations were run using a high performance computation (HPC) system that has an Intel(R) Xeon(R) Gold 6154 CPU with a 3.0 GHz 36 core processor and 768 GB of memory and a conventional laptop that has an Intel(R) Core(TM) i7-4600U CPU with a 2.10 GHz dual-core processor and 12 GB of memory. For each model (M1–M4) we ran the SimNIBS coil position/orientation optimization procedure to maximize $\langle \|\mathbf{E}(\mathbf{r})\| \rangle$ and ADM to maximize $\|\langle \mathbf{E}(\mathbf{r}) \rangle\|$. Fig. 7 shows computational times required as a function of total candidate coil positions and orientations. On the high performance computation system, the SimNIBS coil placement optimization requires on average 7 seconds per candidate configuration, whereas our approach requires an average total time of 7 minutes and 15 seconds regardless of the number of candidate

configurations. As such, a SimNIBS optimization with 10,000 candidate coil placements takes 20 hours, whereas ADM is 165 times faster, taking a little over 7 minutes. The memory required to run the SimNIBS optimization ranged 11–11.5 GB, whereas with ADM it was 6.3 – 6.5 GB. Note the memory requirements of SimNIBS can be lowered to 3.5 GB by using their iterative solver for the optimization [43], which, however, takes significantly longer. We decided not to use the SimNIBS iterative solver because many current laptop computers may have 16 GB of memory and, thus, memory requirements do not impede coil position and orientation optimization. In Fig. 7B, additional computational runtime results for the ADM are shown. Computational time starts to increase beyond 100 thousand coil placements. The total time to run 1 million coil placements was 15 minutes, whereas assuming 7 seconds per simulation, with the SimNIBS approach it would have taken approximately 8 days.

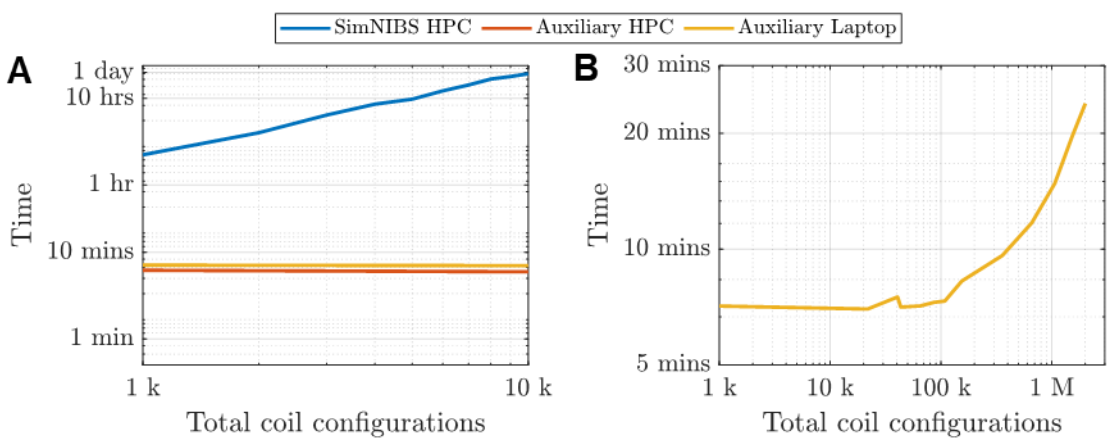


Figure 7. CPU run-time vs number of total coil configurations. (A) Results for SimNIBS and ADM. (B) Extended results for ADM. CPU run-times are averaged across models M1–M4.

*Coil position and orientation application*

Fig. 8 shows results for M1–M4 using SimNIBS to maximize $\langle \|\mathbf{E}(\mathbf{r})\| \rangle$ and ADM to maximize $\|\langle \mathbf{E}(\mathbf{r}) \rangle\|$. Except for M3 and its 1 mm diameter ROI, and 4 cm diameter ROI results, all of the coil placement optimizations result in the same position and differ in orientation by less than 2°. For M3 and 1 mm diameter ROI, the optimum coil position computed by our inhouse direct method and the ADM approach are identical (supplement Fig. S6) indicating that the 3.3 mm distance

between the optimum of simNIBS and ADM are likely due to numerical errors. For ROIs with 4 cm diameter, the discrepancy between ADM and simNIBS optimum TMS coil position is likely due to inaccuracies in the approximation of the E-field magnitude using ADM. For regions with diameter below 4 cm, the orientation differences are likely because ADM was run with an angular step size of 1°, whereas the SimNIBS simulations were run with an angular step size of 5° (due to long computation times). As such, the observed differences in coil orientation between ADM and SimNIBS are below the resolution of our optimization.

In Fig. 8, $\hat{\mathbf{t}}_{\mathbf{opt}}$ is shown for each ROI. $\hat{\mathbf{t}}_{\mathbf{opt}}$ is always perpendicular to a sulcal wall of the ROI. This is consistent with what has been found experimentally [14,18,19]. Whenever there are multiple bends in the ROI it is difficult to identify the precise normal to the sulcal wall. Our framework helps disambiguate a precise coil orientation that should be used.

In a conventional neuronavigated coil placement protocol the coil would have been placed directly above the center of mass ($\mathbf{R}_{\mathbf{CM}}$) and oriented to generate a primary E-field along $\hat{\mathbf{t}}_{\mathbf{opt}}$ (i.e. $\widehat{\mathbf{O}}_{\mathbf{CM}} = \hat{\mathbf{t}}_{\mathbf{opt}}$) [Fig.8]. Fig. 9 compares conventional neuronavigated coil placement and optimization approaches. The E-fields dose obtained by conventional coil placement approaches can be up to 6.0 % lower than the E-field guided ones [Fig. 9A-B]. The E-fields achieved by each optimum coil placement strategy are almost identical and differ by less than 0.3 % [Fig. 9C]. The coil positions obtained by neuronavigated approaches and optimized ones can vary as much as 13.8 mm. Furthermore, between the two optimization objectives the coil positions at most differ by 3.2 mm. The ADM method to optimize $\|\langle \mathbf{E}(\mathbf{r})\rangle\|$ results in nearly the same optimum performance and location as using SimNIBS to optimize $\langle\|\mathbf{E}(\mathbf{r})\|\rangle$. Also, improvements in efficacy of TMS could be achieved over placing the coil directly above the ROI by using the ADM method.

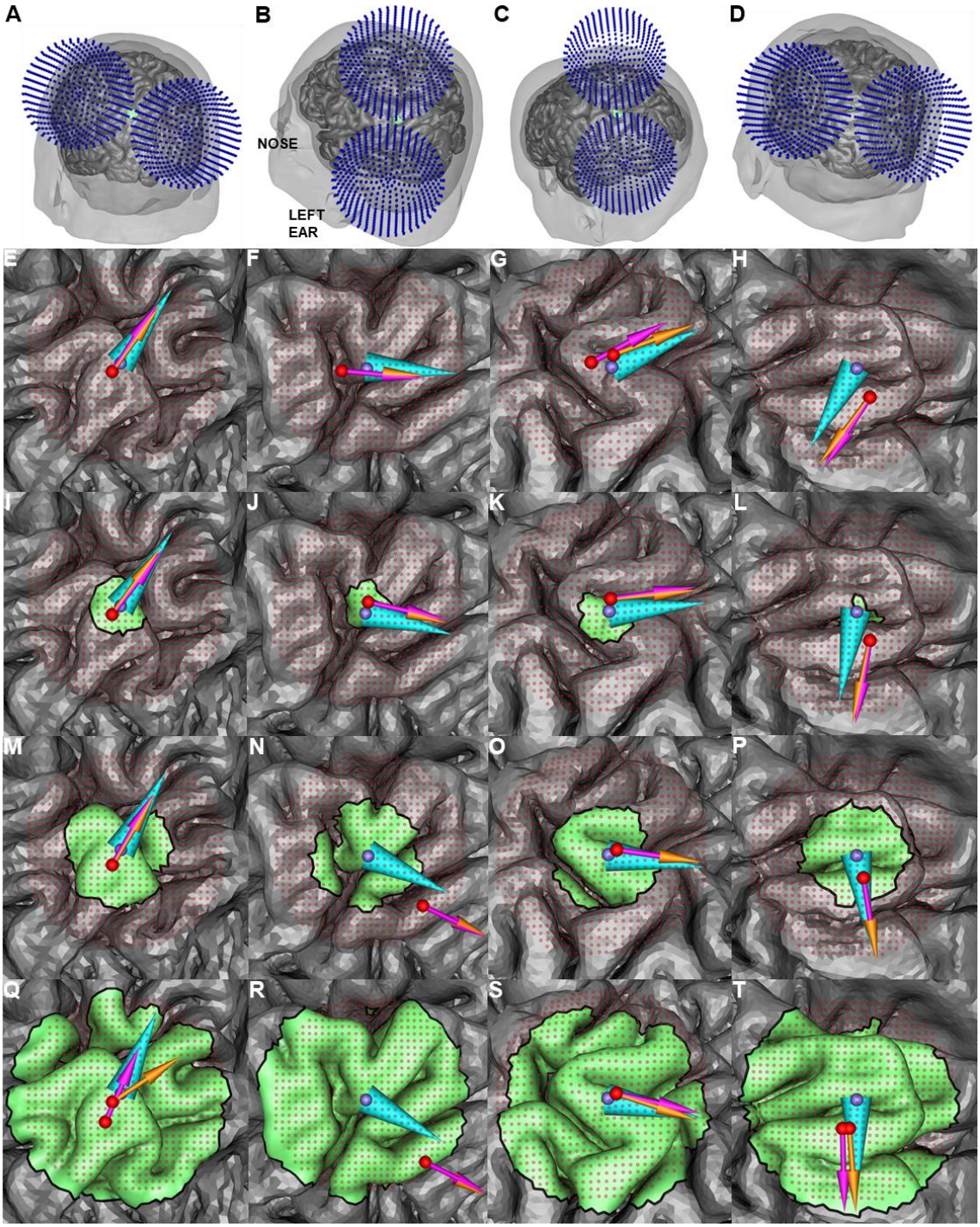


Figure 8. Coil placement results for M1-M4 for ROIs of varying sizes. ADM optimized setup for the 1 cm diameter ROI for (A) M1, (B) M2, (C) M3, and (D) M4.In (E)-(T) the SimNIBS and ADM optimized position and orientation are represented by purple and orange arrow, respectively, $\hat{\mathbf{t}}_{\mathbf{opt}}$ and the ROI CM are represented by the cyan cone and purple sphere, respectively. Columns left to right have results for M1 through M4. Each row top to bottom has results with increasing ROI diameter 1, 10, 20, 40 mm. In most cases both optimization methods result in the same coil position and orientation (indicated by orange arrow head but magenta arrow stem) or similar optimal results.

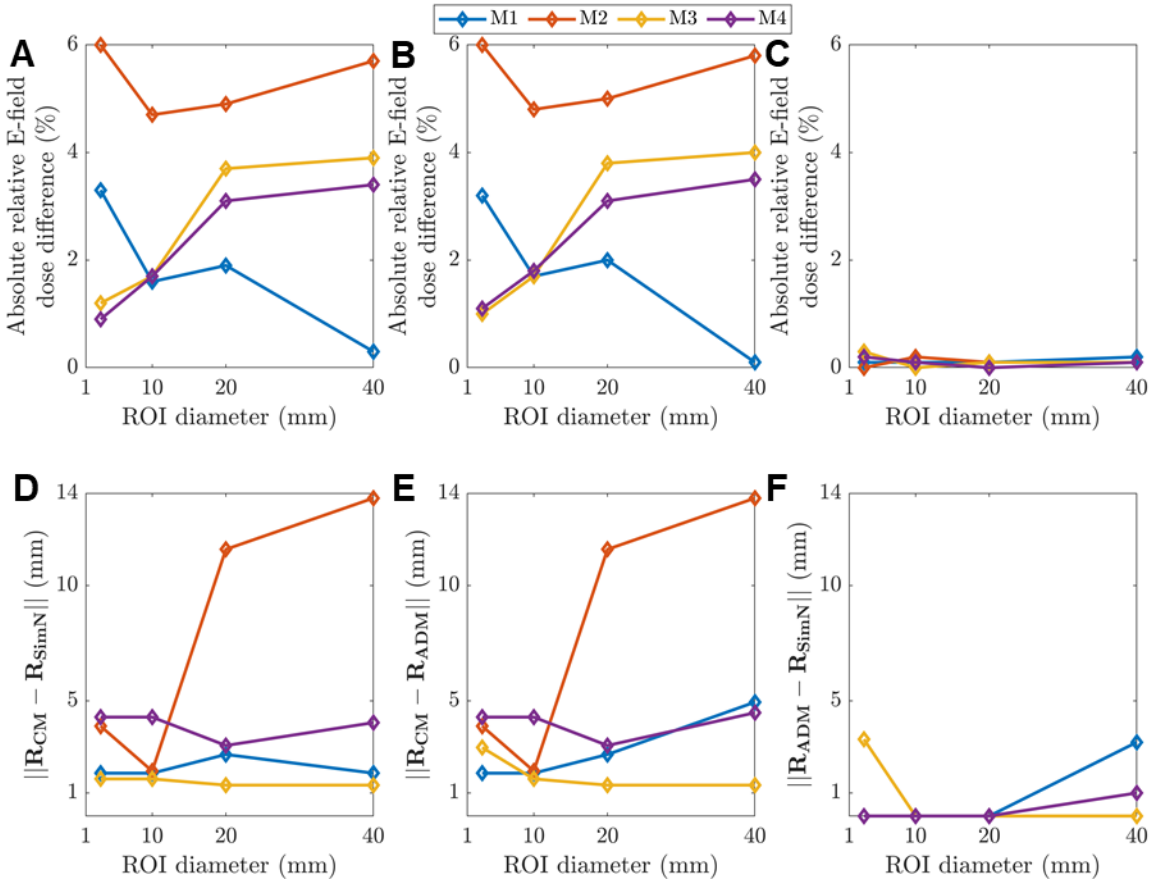


Figure 9. Comparisons between coil positioning strategies in terms of position and induced E-field dose for ROIs of varying sizes. The absolute relative E-field dose achieved by placing the coil (A) above the CM ($\mathbf{R}_{\mathbf{CM}}$) and at the optimum coil position found by SimNIBS ($\mathbf{R}_{\mathbf{SimN}}$), (B) $\mathbf{R}_{\mathbf{CM}}$ and optimum found by ADM ($\mathbf{R}_{\mathbf{ADM}}$) and (C) $\mathbf{R}_{\mathbf{SimN}}$ and $\mathbf{R}_{\mathbf{ADM}}$. Distance between coil placements (D) $\mathbf{R}_{\mathbf{CM}}$ and $\mathbf{R}_{\mathbf{SimN}}$, (E) $\mathbf{R}_{\mathbf{CM}}$ and $\mathbf{R}_{\mathbf{ADM}}$, and (F) $\mathbf{R}_{\mathbf{ADM}}$ and $\mathbf{R}_{\mathbf{SimN}}$. Additional coil optimization comparisons given in Tables S1 and S2 in the supplemental material.

*Coil placement uncertainty quantification application*

As an example, we computed the uncertainty in $|\langle \mathbf{E}(\mathbf{r}) \cdot \hat{\mathbf{t}} \rangle|$ for the 10 mm diameter ROI in the head model M2 resulting from coil position and orientation uncertainty. Fig. 10 shows results for various levels of coil position uncertainty. For fixed $R_\Delta$ the minimum of the standard deviation is seen where the expected value of the E-field is highest, and the standard deviation at each position increases with $R_\Delta$. For fixed $R_\Delta$ the expected value decreases monotonically away from its optimum, and this decrease accelerates with increasing $R_\Delta$. In Fig. 11, we plotted the 90% confidence interval and expected value for $|\langle \mathbf{E}(\mathbf{r}) \cdot \hat{\mathbf{t}} \rangle|$ for various levels of position and orientation uncertainty. The expected value of $|\langle \mathbf{E}(\mathbf{r}) \cdot \hat{\mathbf{t}} \rangle|$ decreases with increased $R_\Delta$. The range of the 90%

confidence interval of $|\langle \mathbf{E}(\mathbf{r}) \cdot \hat{\mathbf{t}} \rangle|$ is nearly doubled if the coil is placed 5 mm away from its optimal position (Fig. 11A-E). Furthermore, coil orientation uncertainty does not significantly contribute to total uncertainty (Fig. 11F). All of these results indicate that errors in identifying optimum coil position both decreases efficacy of TMS and also increases uncertainty in the TMS induced E-field due possible coil positioning errors. Furthermore, it is more critical to identify the optimum coil positioning whenever there are large coil positioning uncertainties associated with the TMS coil placement protocol.

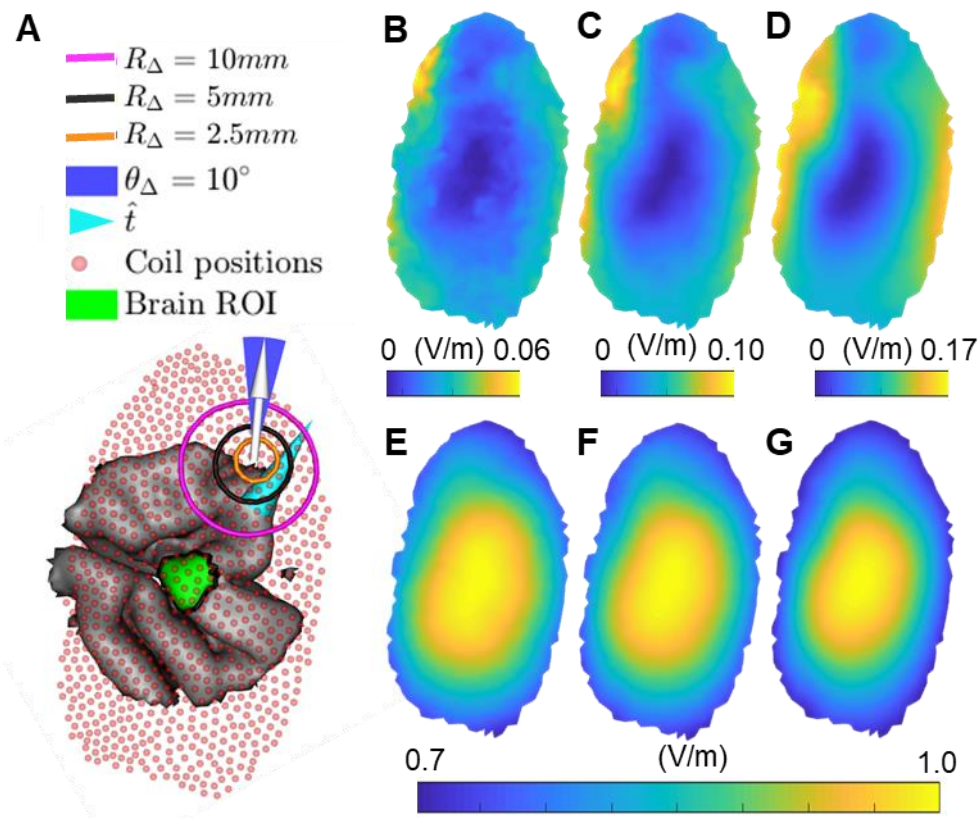


Figure 10. Coil position uncertainty results for model M2 and 1 cm diameter ROI. (A) Coil placements are chosen on the scalp above the brain ROI, and the maximum of the expected value and standard deviation for the average E-field along $\hat{\mathbf{t}}$ for each coil position is determined. Coil is oriented along white vector and orientation uncertainty is always chosen as $\theta_\Delta = 10°$. A typical support for coil position uncertainty for $R_\Delta = 2.5\ mm$, $R_\Delta = 5.0\ mm$, and $R_\Delta = 10\ mm$ is the region enclosed by the orange, black, and magenta circles. (B–D) The standard deviation assuming a coil position uncertainty of (B) 2.5 mm, (C) 5 mm, and (D) 10 mm. (E–G) The expected value for the average E-field assuming a coil position uncertainty $R_\Delta$ of (E) 2.5 mm, (F) 5 mm, and (G) 10 mm. Results are normalized by the maximum expected average E-field over all coil positions and orientations.

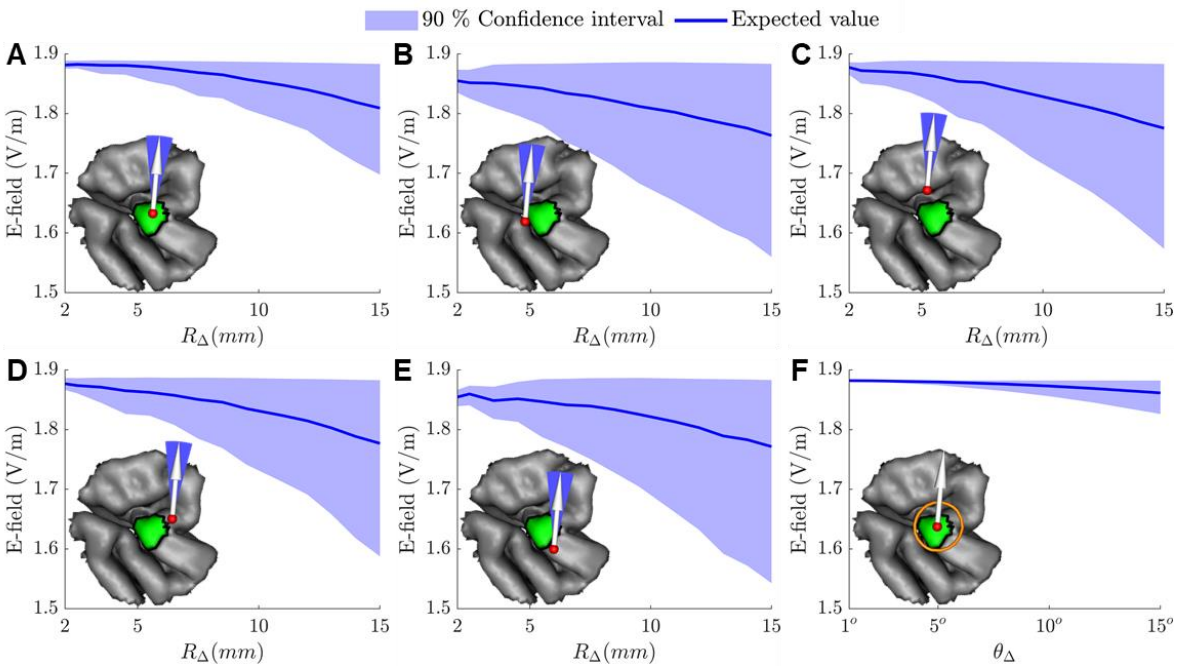


Figure 11. 90 % confidence region of marginal distributions and expected value of the average E-field in the ROI as a function of coil position and orientation uncertainty. (A–E) Results are shown assuming $\theta_\Delta = 10°$ and the coil is positioned (A) centered or (B–E) 5 mm off-center relative to the ROI. (F) Results are shown assuming $R_\Delta = 5$ mm and the coil is centered above the ROI.

## Discussion and Conclusion

ADM, which uses auxiliary dipoles along with electromagnetic reciprocity, enables rapid extraction of optimal coil position and orientation to target the TMS E-field to specific brain regions. Furthermore, ADM enables the rapid quantification of uncertainty of TMS induced ROI E-fields resulting from uncertainty in the coil position and orientation. The validation results indicate that the average E-field along a given direction in an ROI can be computed with a numerical error below 1% using ADM with 578 dipoles. For ROIs with diameters below 2 cm, the average magnitude of the E-field can be estimated to an error below 2% by executing ADM only three times, corresponding to three orthogonal spatial directions of the E-field. As such, ADM can accurately determine the optimal coil placement based on maximization of either the E-field along a given direction or the E-field magnitude for typical cortical ROIs.

The optimal coil positions and orientations determined via ADM and the direct FEM approach for maximizing the average E-field are virtually identical for ROIs with diameter below 2 cm. To optimize the coil placement for one subject, computations take over two days using FEM, whereas ADM runs in under 15 minutes on a laptop. Thus, ADM is a practical rapid method for E-field-informed coil placement.

The difference between the location on the scalp closest to the targeted ROI center of mass and the E-field-informed optimum coil placement is between 1 to 14 mm consistent with prior results using direct simulations that observed an average distance of 5.5 mm and as high as 1.2 cm for ROIs on the temporal brain region [14]. When the objective is to maximize the E-field magnitude in the ROI, the optimal coil orientation is ambiguous for ROIs containing highly curved sulcal walls. The reciprocity-based approach and ADM provide a fast-computational method that can address all of these issues by enabling E-field-informed coil placement to be done on a standard laptop.

## Conflict of interest declaration

The authors declare that there is no conflict of interest regarding the publication of this article.

## Acknowledgement

Research reported in this publication was supported by the National Institute of Mental Health and the National Institute on Aging of the National Institutes of Health under Award Numbers K99MH120046, RF1MH114268, RF1MH114253, and U01AG050618. The content of current research is solely the responsibility of the authors and does not necessarily represent the official views of the National Institutes of Health.

# Supplemental Material

*Reciprocity method applied to magnetic dipole coil models*

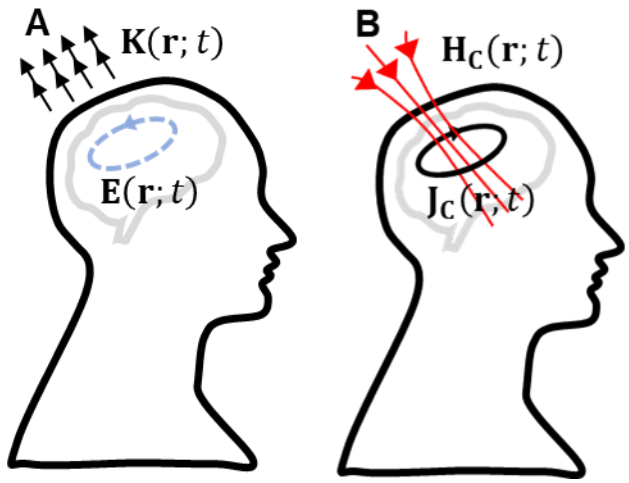


Figure S1. Reciprocal scenarios: (A) Magnetic dipoles generates an E-field inside the cortex, and (B) a cortical source generates an H-field where the magnetic dipoles reside.

Here the reciprocity section of the main text is repeated with appropriate field related quantities replaced for magnetic dipole coil model application. Reciprocity is an equivalence relationship between two scenarios (Fig. S1). In one scenario, the TMS coil, modeled as impressed magnetic currents $\mathbf{K}(\mathbf{r};t) = p'(t)\mathbf{K}(\mathbf{r})$, generates and E-field $\mathbf{E}(\mathbf{r};t) = p'(t)\mathbf{E}(\mathbf{r})$ inside the head (Fig. S1A). In the second scenario, a source $\mathbf{J_C}(\mathbf{r};t) = p(t)\mathbf{J_C}(\mathbf{r})$ inside the head generates H-field $\mathbf{H_C}(\mathbf{r};t) = p(t)\mathbf{H_C}(\mathbf{r})$ (Fig. S1B). Reciprocity dictates that the reaction integral between $\mathbf{E}(\mathbf{r};t)$ and $\mathbf{J_C}(\mathbf{r};t)$ is equal to the reaction integral between $\mathbf{K}(\mathbf{r};t)$ and $\mathbf{H_C}(\mathbf{r};t)$. In other words,

$$\int \mathbf{E}(\mathbf{r};\mathrm{t}) \cdot \mathbf{J_C}(\mathbf{r};\mathrm{t})\mathrm{d}\mathbf{r} = -\int \mathbf{H_C}(\mathbf{r};\mathrm{t}) \cdot \mathbf{K}(\mathbf{r};\mathrm{t})\mathrm{d}\mathbf{r} \quad . \tag{S1}$$

Here we choose $\mathbf{J_C}(\mathbf{r};t) = 0$ outside of the ROI and $\mathbf{J_C}(\mathbf{r};t) = p(t)V_{ROI}^{-1}\hat{\mathbf{t}}$ inside it. Reciprocity results in the following equation for the average E-field along $\hat{\mathbf{t}}$ in the ROI

$$\langle \mathbf{E}(\mathbf{r}) \cdot \hat{\mathbf{t}} \rangle = -\int \mathbf{H_C}(\mathbf{r}) \cdot \mathbf{K}(\mathbf{r})\mathrm{d}\mathbf{r} \quad . \tag{S2}$$

(Note: the temporal variation has been factored out in this equation. Furthermore, in what follows the temporal variation of all currents and E-fields is $p(t)$ and $p'(t)$, respectively, and it is

suppressed in the notation.)

Computing $\langle \mathbf{E}(\mathbf{r}) \cdot \hat{\mathbf{t}} \rangle$ using Eq. (S2) requires the evaluation of $\mathbf{H}_\mathbf{C}(\mathbf{r})$ outside of the conductive head. This is done by computing the primary H-field due to the cortical current $\mathbf{J}_\mathbf{C}(\mathbf{r})$, and secondary H-field due to conduction currents $\overline{\overline{\boldsymbol{\sigma}}}(\mathbf{r})\mathbf{E}_\mathbf{C}(\mathbf{r})$, where $\overline{\overline{\boldsymbol{\sigma}}}(\mathbf{r})$ is the conductivity tensor inside the head. This results in the following

$$\mathbf{H}_\mathbf{C}(\mathbf{r}) = \frac{1}{4\pi} \nabla \times \int_{\text{Head}} \frac{\mathbf{J}_\mathbf{C}(\mathbf{r}') + \overline{\overline{\boldsymbol{\sigma}}}(\mathbf{r}')\mathbf{E}_\mathbf{C}(\mathbf{r}')}{\|\mathbf{r} - \mathbf{r}'\|} \mathrm{d}\mathbf{r}' \ . \tag{S3}$$

Finally, to estimate Eqs. (S2)–(S3) we use the same approach as described in the manuscript to estimate Eqs. (2)–(3). Specifically, in Eqs. (5)–(6) become

$$\mathbf{H}_\mathbf{C}(\mathbf{r}) = -\frac{1}{4\pi} \sum_{j=1}^{N} \mathbf{J}_\mathbf{C}^{(j)} \times \nabla \frac{1}{\left\| \mathbf{r} - \mathbf{r}_\mathbf{C}^{(j)} \right\|} \quad , \tag{S4}$$

and, assuming the coil model consists of magnetic dipoles $\mathbf{K}_\mathbf{coil}^{(i)}$ at locations $\mathbf{r}_\mathbf{coil}^{(i)}$ , where $i = 1,2,\ldots,M$,

$$\langle \mathbf{E}(\mathbf{r}) \cdot \hat{\mathbf{t}} \rangle = \frac{1}{4\pi} \sum_{i=1}^{M} \mathbf{K}_\mathbf{coil}^{(i)} \cdot \sum_{j=1}^{N} \mathbf{J}_\mathbf{C}^{(j)} \times \nabla \frac{1}{\left\| \mathbf{r}_\mathbf{coil}^{(i)} - \mathbf{r}_\mathbf{C}^{(j)} \right\|} \, . \tag{S5}$$

*Auxiliary dipole approximation*

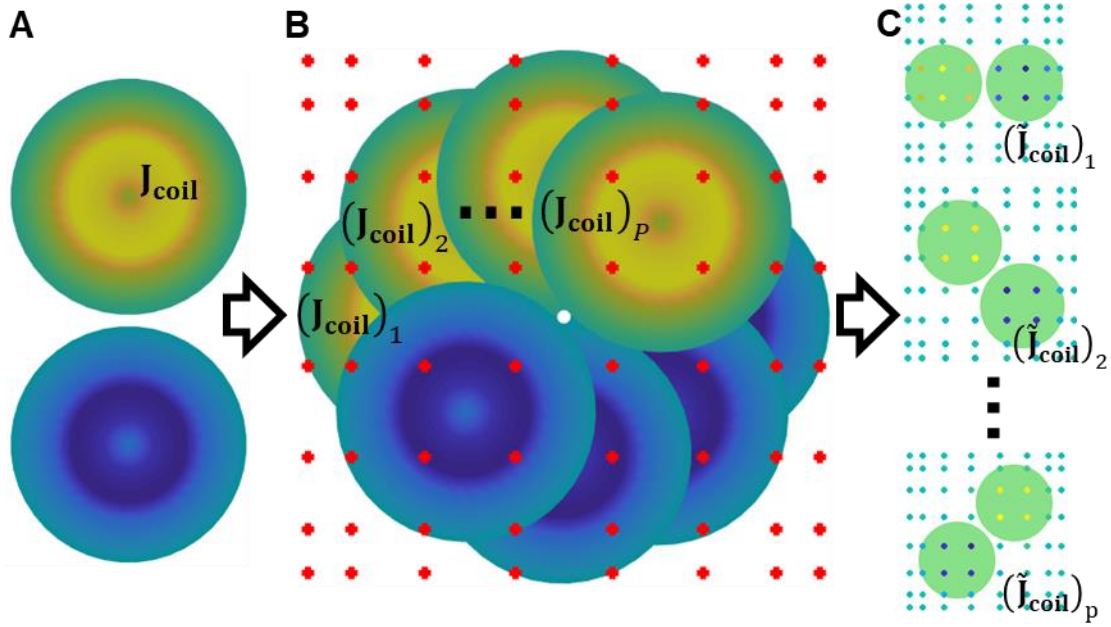


Figure S2. Auxiliary dipole method workflow. (A) TMS coil dipole model. (B) TMS coil dipole model having different orientations and embedded in a grid of Gauss-Legendre nodes. (C) Dipole weights for individual coil orientations.

Here we describe the procedure used to approximate all coil orientations using a few dipoles located at auxiliary nodes (Fig. S2). The dipoles are chosen as Gauss-Legendre tensor product nodes of a rectangular box enclosing the coil (Fig. S2B). Assume that the x-y axis is chosen as the coil plane, and it consists of $M$ dipoles $\mathbf{J}_{\mathbf{coil}}^{(i)}$ at locations $\mathbf{r}_{\mathbf{coil}}^{(i)}$, where $\mathrm{i} = 1,2,\ldots M$ (Fig. S2A). From $\mathbf{J}_{\mathbf{coil}}^{(\mathrm{i})}$ and $\mathbf{r}_{\mathbf{coil}}^{(\mathrm{i})}$, we generate $P$ coil dipole models $\left(\mathbf{J}_{\mathbf{coil}}^{(i)}\right)_j$ at locations $\left(\mathbf{r}_{\mathbf{coil}}^{(i)}\right)_j$ and $j = 1,2,\ldots P$, by rotating $\mathbf{J}_{\mathbf{coil}}^{(i)}$ and $\mathbf{r}_{\mathbf{coil}}^{(i)}$ (Fig. S2B). Assume that all the coil models can be bound by a box $\Omega_{\mathrm{box}} = [-x_{coil}, x_{coil}] \times [-y_{coil}, y_{coil}] \times [-z_{coil}, z_{coil}]$ outside of the head. For each coil orientation, we need to compute

$$\frac{1}{4\pi}\sum_{i=1}^{M}\left(\mathbf{J}_{\mathbf{coil}}^{(i)}\right)_j \cdot \mathbf{E}_{\mathbf{C}}\left(\left(\mathbf{r}_{\mathbf{coil}}^{(i)}\right)_j\right) \quad , \tag{S6}$$

Since $\Omega_{\mathrm{box}}$ is outside of the head, $\mathbf{E}_{\mathbf{C}}\left(\left(\mathbf{r}_{\mathbf{coil}}^{(i)}\right)_j\right)$ is interpolated using a polynomial defined from samples in $\Omega_{\mathrm{box}}$ with an error that decreases exponentially with number of points. We

approximate $\mathbf{E_C}\left(\left(\mathbf{r}_{\mathbf{coil}}^{(i)}\right)_j\right) \approx \sum_{k=1}^{L} \mathbf{E_C}\left(\tilde{\mathbf{r}}_{\mathbf{coil}}^{(k)}\right) \phi_k\left(\left(\mathbf{r}_{\mathbf{coil}}^{(i)}\right)_j\right)$ , where positions $\tilde{\mathbf{r}}_{\mathbf{coil}}^{(k)}$ are chosen from tensor product rules of Legendre-gauss quadrature on $\Omega_{\mathrm{box}}$ and $\phi_k$ are chosen as Lagrange polynomials. Plugging in the approximation to Eq. (S6) results in the following

$$\begin{gathered}\frac{1}{4\pi}\sum_{i=1}^{M}\left(\mathbf{J}_{\mathbf{coil}}^{(i)}\right)_j \cdot \mathbf{E_C}\left(\left(\mathbf{r}_{\mathbf{coil}}^{(i)}\right)_j\right) \approx \frac{1}{4\pi}\sum_{k=1}^{L}\left(\tilde{\mathbf{J}}_{\mathbf{coil}}^{(k)}\right)_j \cdot \mathbf{E_C}\left(\tilde{\mathbf{r}}_{\mathbf{coil}}^{(k)}\right) \\ \left(\tilde{\mathbf{J}}_{\mathbf{coil}}^{(k)}\right)_{\mathrm{j}} = \sum_{i=1}^{M}\left(\mathbf{J}_{\mathbf{coil}}^{(i)}\right)_j \cdot \phi_k\left(\left(\mathbf{r}_{\mathbf{coil}}^{(i)}\right)_j\right)\end{gathered} . \tag{S7}$$

In Eq. (8), all of the coil orientations share the same dipole locations enabling the batch evaluation of $\mathbf{E_{avg}}$ (Fig. S2C). Note: Eq. (S7) only incorporates information about the Lagrange interpolating polynomial functions, as such, it remains valid for magnetic dipole models without modification.

*SimNIBS validation simulation results*

Here additional validation results are given indicating that our implementation achieves comparable error levels to SimNIBS, a commonly used non-invasive brain stimulation E-field dosimetry toolbox. In Fig. S3 we show Spherical head model results. The errors observed for the spherical head are slightly higher than our direct FEM. These small differences in accuracy are likely due to differences in the way that the primary E-field is computed. In Fig. S4 we compare the results obtained for the Ernie head model via our direct FEM with SimNIBS. The maximum relative difference across all simulations was 0.11 %. In Fig. S5 we compare results obtained for the four additional subjects obtained via our direct FEM and SimNIBS. The agreement between the two sets of solutions increases with ROI size. This is likely because we compute the average the E-field on the ROI, which is less sensitive to numerical errors with increasing ROI size. In all cases SimNIBS was in agreement with our direct FEM to a fraction of a percentage indicating that both codes result in virtually the same solution.

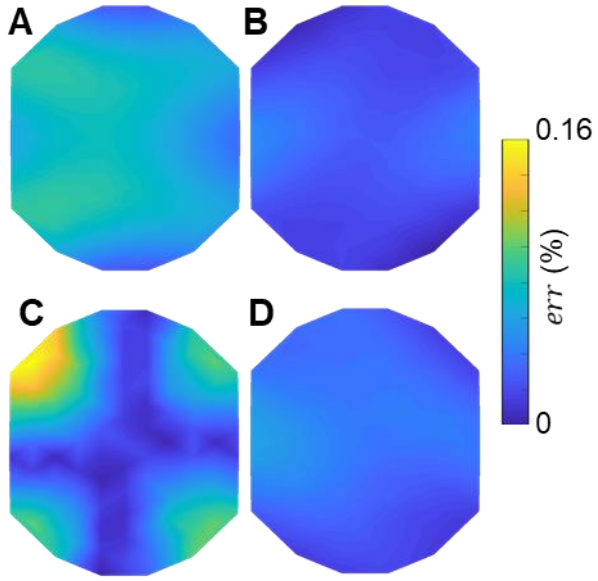


Figure S3. Sphere head model SimNIBS simulation results. The $err$ observed at each scalp location for coil orientations of (A) 0°, (B) 45°, (C) 90°, and (D) 135°.

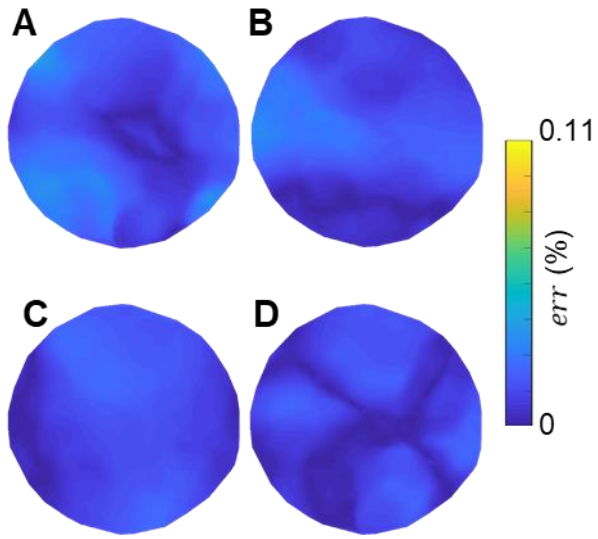


Figure S4. Ernie head model SimNIBS simulation results. The $err$ observed at each scalp location for coil orientations of (A) 0°, (B) 45°, (C) 90°, and (D) 135°. The direct FEM is used as a reference solution.

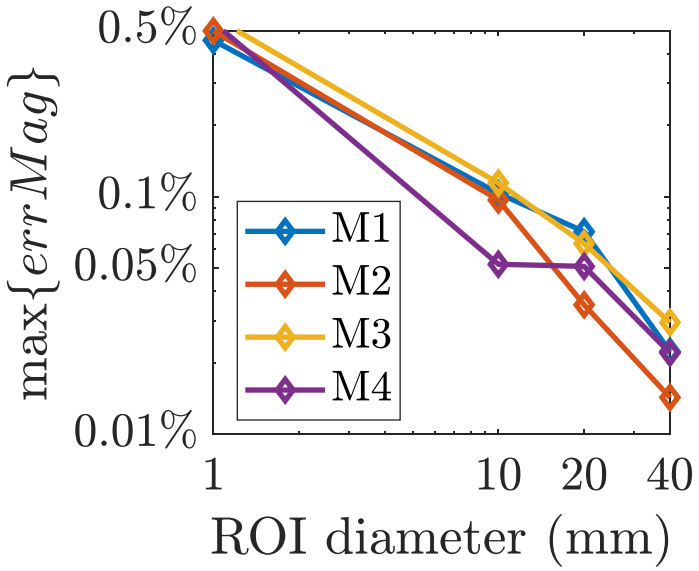


Figure S5. Maximum normalized relative difference for the average E-field magnitude on four additional subjects. The direct FEM is used as a reference solution.

*Additional coil placement and orientation results*

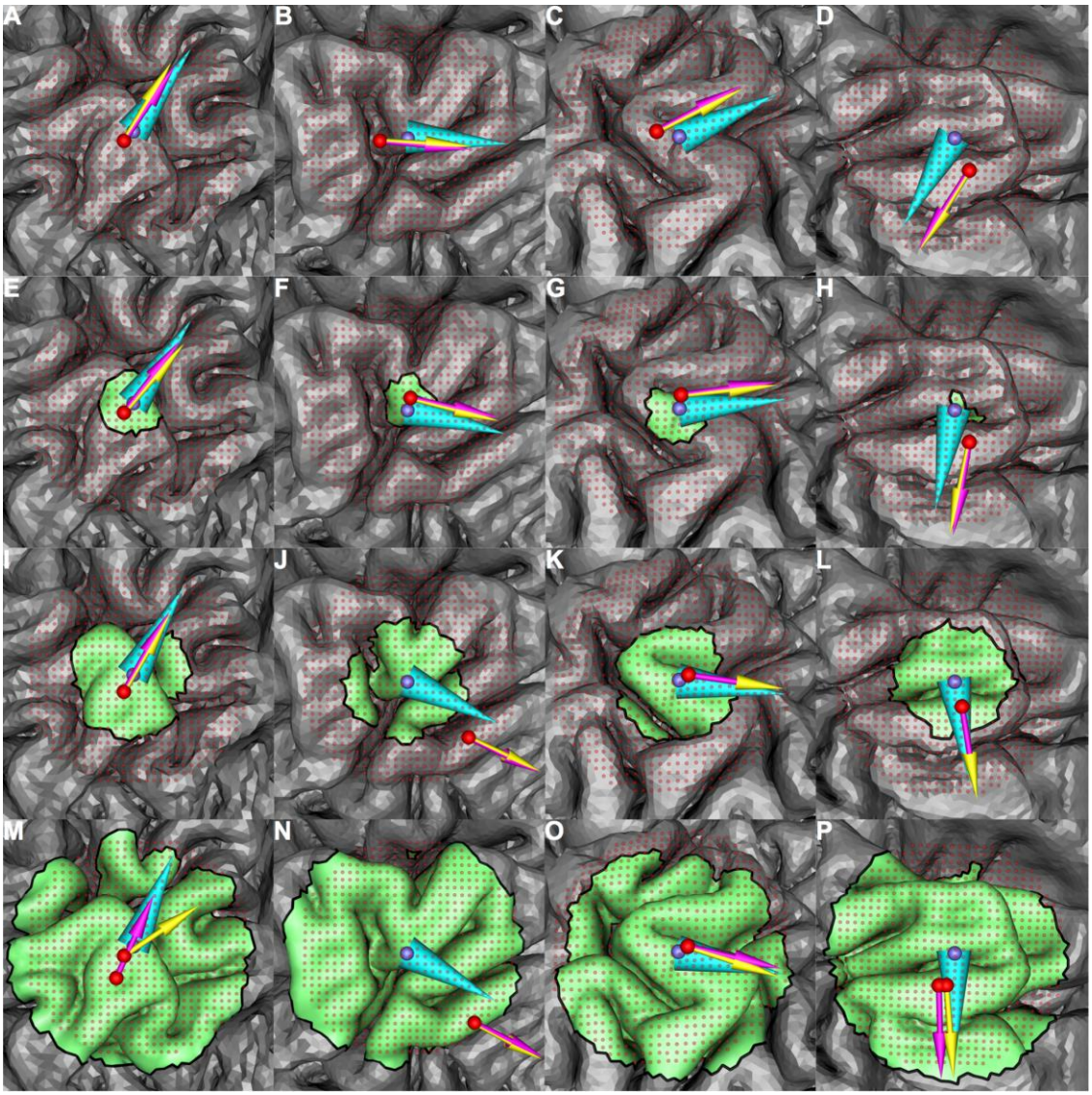


Figure S6. Coil placement results for M1–M4 for ROIs of varying sizes. In (A)–(P) the in-house FEM optimized and ADM optimized position and orientation are represented by the purple and yellow arrow, respectively, $\hat{\mathbf{t}}_{\mathbf{opt}}$ and the ROI CM are represented by the cyan cone and purple sphere, respectively. Columns left to right have results for M1 through M4. Each row top to bottom has results with increasing ROI diameter 3 (1 tetrahedron), 10, 20, 40 mm. In most cases both optimization methods result in the same coil position and orientation (indicated by yellow arrow head but magenta arrow stem) or similar optimal results.

| Model-RadiusROI | $\lVert \mathbf{R_{CM}} - \mathbf{R_{simN}} \rVert$ [mm] | $\lvert \theta_{CM} - \theta_{simN} \rvert$ [°] | $\left( \frac{\langle \lVert \mathbf{E_{CM}}(\mathbf{r}) \rVert \rangle}{\langle \lVert \mathbf{E_{simN}}(\mathbf{r}) \rVert \rangle} - 1 \right)$ %[V/m] | $\lVert \mathbf{R_{CM}} - \mathbf{R_{ADM}} \rVert$ [mm] | $\lvert \theta_{CM} - \theta_{ADM} \rvert$ [°] | $\left( \frac{\lVert \langle \mathbf{E_{CM}}(\mathbf{r}) \rangle \rVert}{\lVert \langle \mathbf{E_{ADM}}(\mathbf{r}) \rangle \rVert} - 1 \right)$ %[V/m] |
|---|---|---|---|---|---|---|
| M1-3mm | 1.86 | 35.7 | -3.04 | 1.86 | 37.7 | -2.89 |
| M1-5mm | 1.86 | 35.7 | -1.58 | 1.86 | 33.7 | -1.53 |
| M1-10mm | 2.67 | 41.1 | -1.87 | 2.67 | 42.1 | -1.62 |
| M1-20mm | **1.86** | 16.0 | -0.26 | **4.94** | 47.5 | **1.83** |
| M2-3mm | 3.90 | 62.0 | **-5.75** | 3.90 | 60.0 | **-5.75** |

| | | | | | | |
|---|---|---|---|---|---|---|
| M2-5mm | 1.95 | 51.0 | -4.71 | 1.95 | 53.0 | -4.80 |
| M2-10mm | 11.57 | 42.0 | -4.88 | 11.57 | 41.0 | -4.62 |
| M2-20mm | **13.79** | 39.0 | -5.73 | **13.79** | 41.0 | -3.46 |
| M3-3mm | 1.61 | 18.1 | -0.91 | **2.97** | 10.7 | -0.63 |
| M3-5mm | 1.61 | 33.1 | -1.66 | 1.61 | 31.1 | -1.30 |
| M3-10mm | 1.34 | 47.3 | -3.67 | 1.34 | 47.3 | -3.15 |
| M3-20mm | 1.34 | 57.3 | -3.93 | 1.34 | 52.3 | -2.81 |
| M4-3mm | 4.29 | 5.92 | -1.08 | 4.29 | 3.97 | -1.30 |
| M4-5mm | 4.29 | 20.9 | -1.67 | 4.29 | 22.9 | -1.38 |
| M4-10mm | 3.06 | 41.7 | -3.02 | 3.06 | 41.7 | -2.39 |
| M4-20mm | **4.05** | 36.9 | -3.41 | **4.48** | 33.8 | -1.52 |

Table S1: Additional comparisons between placing the coil above the scalp and where it maximizes the ROI E-field. Note: E-field dose here is compared according to the prediction given by the respective algorithm: $\langle \|\cdot\| \rangle$ for SimNIBS comparisons and $\|\langle \cdot \rangle\|$ for ADM comparisons.

| Model-RadiusROI | $\|\mathbf{R_{ADM}} - \mathbf{R_{simN}}\|$ [mm] | $\|\theta_{ADM} - \theta_{simN}\|$ [°] | $\left(\frac{\|\langle \mathbf{E_{ADM}}(\mathbf{r}) \rangle\|}{\langle \|\mathbf{E_{simN}}(\mathbf{r})\| \rangle} - 1\right)$ (%) [V/m] |
|---|---|---|---|
| M1-1mm | 0.00 | 2 | -0.15 |
| M1-5mm | 0.00 | 2 | -0.049 |
| M1-10mm | 0.00 | 1 | -0.25 |
| M1-20mm | 3.20 | 32 | -2.1 |
| M2-1mm | 0.00 | 2 | -0.0035 |
| M2-5mm | 0.00 | 2 | 0.095 |
| M2-10mm | 0.00 | 1 | -0.28 |
| M2-20mm | 0.00 | 2 | **-2.4** |
| M3-1mm | **3.33** | 7.6 | -0.28 |
| M3-5mm | 0.00 | 2 | -0.36 |
| M3-10mm | 0.00 | 0 | -0.54 |
| M3-20mm | 0.00 | 5 | -1.2 |
| M4-1mm | 0.00 | 4 | 0.23 |
| M4-5mm | 0.00 | 2 | -0.3 |
| M4-10mm | 0.00 | 0 | -0.65 |
| M4-20mm | 1.00 | 3.25 | -1.9 |

Table S2: Additional comparisons between maximizing E-field magnitude (i.e. maximize $\langle \|\cdot\| \rangle$) and using ADM to approximately maximize E-field magnitude (i.e. maximize $\|\langle \cdot \rangle\|$). Unlike in the main text and Table S1 we compare E-field dose predictions using their respective methods to emphasize that the E-field magnitude approximation $\|\langle \cdot \rangle\|$ gives a good estimate of actual E-field magnitude.

# References


[1] Paulus W, Peterchev AV, Ridding M. Transcranial electric and magnetic stimulation: technique and paradigms. In: Handbook of clinical neurology. Vol 116: Elsevier; 2013: 329-42.

[2] Barker AT, Jalinous R, Freeston IL. Non-invasive magnetic stimulation of human motor cortex. The Lancet 1985;325:1106-7.

[3] Bungert A, Antunes A, Espenhahn S, Thielscher A. Where does TMS stimulate the motor cortex? Combining electrophysiological measurements and realistic field estimates to reveal the affected cortex position. Cerebral Cortex 2017;27:5083-94.

[4] Aberra AS, Wang B, Grill WM, Peterchev AV. Simulation of transcranial magnetic stimulation in head model with morphologically-realistic cortical neurons. Brain stimulation 2020;13:175-89.

[5] NIH. RFA-MH-17-600: early stage testing of pharmacologic or device-based interventions for the treatment of mental disorders (R61/R33). 2017.

[6] Herwig U, Padberg F, Unger J, Spitzer M, Schönfeldt-Lecuona C. Transcranial magnetic stimulation in therapy studies: examination of the reliability of “standard” coil positioning by neuronavigation. Biological Psychiatry 2001;50:58-61.

[7] Sack AT, Kadosh RC, Schuhmann T, Moerel M, Walsh V, Goebel R. Optimizing functional accuracy of TMS in cognitive studies: a comparison of methods. Journal of Cognitive Neuroscience 2009;21:207-21.

[8] George MS, Wassermann EM, Williams WA, Callahan A, Ketter TA, Basser P, et al. Daily repetitive transcranial magnetic stimulation (rTMS) improves mood in depression. Neuroreport: An International Journal for the Rapid Communication of Research in Neuroscience 1995.

[9] Pascual-Leone A, Rubio B, Pallardó F, Catalá MD. Rapid-rate transcranial magnetic stimulation of left dorsolateral prefrontal cortex in drug-resistant depression. The Lancet 1996;348:233-7.

[10] Herwig U, Satrapi P, Schönfeldt-Lecuona C. Using the International 10-20 EEG System for Positioning of Transcranial Magnetic Stimulation. Brain Topography 2003;16:95-9.

[11] Gerloff C, Corwell B, Chen R, Hallett M, Cohen LG. Stimulation over the human supplementary motor area interferes with the organization of future elements in complex motor sequences. Brain: a journal of neurology 1997;120:1587-602.

[12] Rusjan PM, Barr MS, Farzan F, Arenovich T, Maller JJ, Fitzgerald PB, et al. Optimal transcranial magnetic stimulation coil placement for targeting the dorsolateral prefrontal cortex using novel magnetic resonance image‐guided neuronavigation. Human brain mapping 2010;31:1643-52.

[13] Deng Z-D, Lisanby SH, Peterchev AV. Electric field depth–focality tradeoff in transcranial magnetic stimulation: simulation comparison of 50 coil designs. Brain stimulation 2013;6:1-13.

[14] Gomez-Tames J, Hamasaka A, Laakso I, Hirata A, Ugawa Y. Atlas of optimal coil orientation and position for TMS: A computational study. Brain stimulation 2018;11:839-48.

[15] Salinas F, Lancaster J, Fox P. 3D modeling of the total electric field induced by transcranial magnetic stimulation using the boundary element method. Physics in medicine and biology 2009;54:3631.
[16] Diekhoff S, Uludağ K, Sparing R, Tittgemeyer M, Cavuşoğlu M, von Cramon DY, et al. Functional localization in the human brain: Gradient‐echo, spin‐echo, and arterial spin‐labeling fMRI compared with neuronavigated TMS. Human brain mapping 2011;32:341-57.
[17] Thielscher A, Opitz A, Windhoff M. Impact of the gyral geometry on the electric field induced by transcranial magnetic stimulation. Neuroimage 2011;54:234-43.
[18] Janssen AM, Oostendorp TF, Stegeman DF. The effect of local anatomy on the electric field induced by TMS: evaluation at 14 different target sites. Medical & biological engineering & computing 2014;52:873-83.
[19] Janssen AM, Oostendorp TF, Stegeman DF. The coil orientation dependency of the electric field induced by TMS for M1 and other brain areas. Journal of neuroengineering and rehabilitation 2015;12:47.
[20] Richter L, Neumann G, Oung S, Schweikard A, Trillenberg P. Optimal Coil Orientation for Transcranial Magnetic Stimulation. PLOS ONE 2013;8:e60358.
[21] Balslev D, Braet W, McAllister C, Miall RC. Inter-individual variability in optimal current direction for transcranial magnetic stimulation of the motor cortex. Journal of neuroscience methods 2007;162:309-13.
[22] Brasil-Neto JP, Cohen LG, Panizza M, Nilsson J, Roth BJ, Hallett M. Optimal focal transcranial magnetic activation of the human motor cortex: effects of coil orientation, shape of the induced current pulse, and stimulus intensity. Journal of clinical neurophysiology: official publication of the American Electroencephalographic Society 1992;9:132-6.
[23] Raffin E, Pellegrino G, Di Lazzaro V, Thielscher A, Siebner HR. Bringing transcranial mapping into shape: sulcus-aligned mapping captures motor somatotopy in human primary motor hand area. Neuroimage 2015;120:164-75.
[24] Goetz SM, Kozyrkov IC, Luber B, Lisanby SH, Murphy DL, Grill WM, et al. Accuracy of robotic coil positioning during transcranial magnetic stimulation. Journal of neural engineering 2019;16:054003.
[25] Sparing R, Buelte D, Meister IG, Pauš T, Fink GR. Transcranial magnetic stimulation and the challenge of coil placement: A comparison of conventional and stereotaxic neuronavigational strategies. Human Brain Mapping 2008;29:82-96.
[26] Ruohonen J, Karhu J. Navigated transcranial magnetic stimulation. Neurophysiologie clinique/Clinical neurophysiology 2010;40:7-17.
[27] Goetz SM, Deng Z-D. The development and modelling of devices and paradigms for transcranial magnetic stimulation. International Review of Psychiatry 2017;29:115-45.
[28] Laakso I, Hirata A. Fast multigrid-based computation of the induced electric field for transcranial magnetic stimulation. Phys. Med. Biol. 2012;57:7753.
[29] Makarov SN, Noetscher GM, Burnham EH, Pham DN, Htet AT, de Lara LN, et al. Software Toolkit for Fast High-Resolution TMS Modeling. bioRxiv 2019:643346.
[30] Dannhauer M, Brooks D, Tucker D, MacLeod R. A pipeline for the simulation of transcranial direct current stimulation for realistic human head models using

SCIRun/BioMesh3D. Engineering in Medicine and Biology Society (EMBC), 2012 Annual International Conference of the IEEE. 2012:5486-9.
[31] Huang Y, Datta A, Bikson M, Parra LC. Realistic vOlumetric-Approach to Simulate Transcranial Electric Stimulation--ROAST--a fully automated open-source pipeline. bioRxiv 2017:217331.
[32] Gomez LJ, Yücel AC, Michielssen E. The ICVSIE: A General Purpose Integral Equation Method for Bio-Electromagnetic Analysis. IEEE Transactions on Biomedical Engineering 2018;65:565-74.
[33] Gomez LJ, Dannhauer M, Koponen LM, Peterchev AV. Conditions for numerically accurate TMS electric field simulation. Brain stimulation 2020;13:157-66.
[34] Thielscher A, Antunes A, Saturnino GB. Field modeling for transcranial magnetic stimulation: A useful tool to understand the physiological effects of TMS? 2015 37th Annual International Conference of the IEEE Engineering in Medicine and Biology Society (EMBC). 2015:222-5.
[35] Makarov SN, Wartman WA, Daneshzand M, Fujimoto K, Raij T, Nummenmaa A. A software toolkit for TMS electric-field modeling with boundary element fast multipole method: An efficient MATLAB implementation. Journal of Neural Engineering 2020.
[36] Beynel L, Davis S, Crowell C, Hilbig S, Lim W, Nguyen D, et al. Online repetitive transcranial magnetic stimulation during working memory in younger and older adults: A randomized within-subject comparison. PloS one 2019;14.
[37] Beynel L, Davis SW, Crowell CA, Dannhauer M, Lim W, Palmer H, et al. Site-specific effects of online rTMS during a working memory task in healthy older adults. Brain Sci 2020;10:255.
[38] Stenroos M, Koponen LM. Real-time computation of the TMS-induced electric field in a realistic head model. NeuroImage 2019;203:116159.
[39] Nummenmaa A, Stenroos M, Ilmoniemi RJ, Okada YC, Hämäläinen MS, Raij T. Comparison of spherical and realistically shaped boundary element head models for transcranial magnetic stimulation navigation. Clinical Neurophysiology 2013;124:1995-2007.
[40] Gimbutas Z, Greengard L. Computational software: Simple fmm libraries for electrostatics, slow viscous flow, and frequency-domain wave propagation. Communications in Computational Physics 2015;18:516-28.
[41] Wolters CH, Grasedyck L, Hackbusch W. Efficient computation of lead field bases and influence matrix for the FEM-based EEG and MEG inverse problem. Inverse problems 2004;20:1099.
[42] Gomez LJ, Dannhauer M, Peterchev AV. https://github.com/luisgo/Auxiliary_Dipole_Method.
[43] Saturnino GB, Madsen KH, Thielscher A. Electric field simulations for transcranial brain stimulation using FEM: an efficient implementation and error analysis. Journal of neural engineering 2019.
[44] Plonsey R, Heppner DB. Considerations of quasi-stationarity in electrophysiological systems. The Bulletin of mathematical biophysics 1967;29:657-64.
[45] Jin J-M. The finite element method in electromagnetics. 3rd Edition ed: John Wiley & Sons; 2014.

[46] Freund RW. A transpose-free quasi-minimal residual algorithm for non-hermitian linear systems. SIAM J. Sci. Stat. Comput. 1993;14:470-82.
[47] Weise K, Numssen O, Thielscher A, Hartwigsen G, Knösche TR. A novel approach to localize cortical TMS effects. Neuroimage 2020;209:116486.
[48] Thielscher A, Kammer T. Electric field properties of two commercial figure-8 coils in TMS: calculation of focality and efficiency. Clinical neurophysiology 2004;115:1697-708.
[49] Crane K, Weischedel C, Wardetzky M. Geodesics in heat: A new approach to computing distance based on heat flow. ACM Transactions on Graphics (TOG) 2013;32:1-11.